Finite-size coherent particle structures in high-Prandtl-number liquid bridges

Ilya Barmak [*]

Institute of Fluid Mechanics and Heat Transfer, TU Wien, 1060 Vienna, Austria
and School of Mechanical Engineering, Tel Aviv University, Tel Aviv 69978, Israel

Francesco Romanò

Univ. Lille, CNRS, ONERA, Arts et Métiers Institute of Technology, Centrale Lille, UMR 9014, LMFL,
Laboratoire de Méchanique des Fluides de Lille, Kampé de Fériet, F-59000, Lille, France

Hendrik C. Kuhlmann

Institute of Fluid Mechanics and Heat Transfer, TU Wien, 1060 Vienna, Austria

The transport of liquid and of small rigid spherical particles in a high-Prandtl-number ($Pr = 68$) thermocapillary liquid bridge under zero gravity is studied by highly resolved numerical simulations when the flow arises as an azimuthally traveling hydrothermal wave with azimuthal wave number one. The Langrangian transport of fluid elements reveals the coexistence of regular and chaotic streamlines in the frame of reference rotating with the wave. The structure of the KAM (Kolmogorov-Arnold-Moser) tori is unraveled for several Reynolds numbers for which the flow is periodic in time and space. Based on the streamline topology the segregation of small rigid spherical particles of a dilute suspension into particle accumulation structures (PASs) is studied, based on the steric finite-particle-size effect when the particles moves close to the free surface. It is shown that the intricate KAM structures have their counterparts in a multitude of different attractors for the particle motion. Examples of PASs are provided, and their dependence on particle size, particle-to-fluid density ratio, and Reynolds number are discussed. A large parametric study reveals the most probable combinations of particle size and density ratio which lead to particle clustering.

I. INTRODUCTION

Particle-laden flows are frequently encountered in natural phenomena [1,2] and industrial applications [3–5]. Therefore, the dynamics of particles suspended in a fluid and their spatial distribution is of fundamental and practical importance [6]. Small rigid particles density matched with the surrounding fluid are of particular interest in experimental fluid mechanics, because they can serve as tracers to visualize the flow or to measure its velocity, assuming they move like the fluid [7]. When dispersed in a thermocapillary liquid bridge, however, even relatively small particles may cluster rapidly along closed threads which rotate in a laminar time-periodic three-dimensional flow. This phenomenon was discovered by Schwabe *et al.* [8] who called the rotating thread a *dynamic particle accumulation structure* (PAS).

Since then, PAS in thermocapillary liquid bridges has received increasing attention both experimentally [9–13] and numerically [14–19]. PAS in a liquid bridge has been experimentally

---
[*]ilya.barmak@tuwien.ac.at

observed only when the flow arises as a three-dimensional azimuthally *traveling* hydrothermal wave (HTW). This type of wave, which emerges from an instability of the steady axisymmetric toroidal vortex flow and its temperature field, has the distinguished property to be dispersion-free. Therefore, a HTW is stationary in a frame of reference which rotates with the same angular velocity as the HTW. The stationary three-dimensional incompressible flow field of the HTW in the rotating frame exhibits two different kinds of streamlines: regular streamlines and chaotic ones [20]. This streamline structure results from the local Hamiltonian system which can be derived from a steady incompressible three-dimensional flow [21]. A regular streamline winds on a closed stream tube which corresponds to a so-called Kolmogorov-Arnold-Moser (KAM) torus. The KAM tori are densely nested around a closed streamline. A set of KAM tori is typically surrounded by chaotic streamlines which extend up to the boundaries of the liquid bridge [14,15].

Hofmann and Kuhlmann [14] showed that PAS relies on the existence of KAM tori which approach the free surface of the liquid bridge very closely. Under this condition particles whose size is comparable to the minimal distance of a KAM torus, or of the closed streamline inside of the set of tori, from the free surface can accumulate in or near the KAM torus. The transfer of a particle, initially moving in the region occupied by chaotic streamlines, to the KAM torus is caused by the extra forces a particle experiences due to its finite size when it is transported close to the free surface. Once a nearly density-matched particle moves near a KAM torus it can hardly escape from it due to the regularity of the motion of the fluid elements contained in the KAM torus. This is the reason why PAS always closely approaches the free surface [9,10]. Since the important processes involved in the creation of PAS rely on the existence of KAM tori and on forces between the particle and the free surface acting on length scales at least as large as the particle size, a numerical analysis of PAS in high-Prandtl-number thermocapillary liquid bridges faces two main difficulties:

1. The first difficulty is the computation of highly resolved strictly periodic flow fields of traveling HTWs and the analysis of these flow fields in terms of their KAM structures. The high resolution is required, because even a small residual divergence of the flow field can lead to accumulation of perfect tracers, thus faking a false attractor which does not exist for the motion of *tracers* in a solenoidal flow field [22].

2. The second difficulty is the accurate computation of the particle motion. Fully resolving the huge range of temporal and spatial scales associated with the moving-boundary problem is prohibitively expensive computationally, even for a single particle. Therefore, currently the particle motion cannot be accurately computed. A remedy may be sought by suitable modeling assumptions which lead to sufficiently accurate approximations of the true particle trajectory.

The higher the Prandtl number, the thinner are the thermal boundary layers in the thermocapillary flow in liquid bridges. Therefore, the accurate computation of the flow field of a HTW (problem 1) becomes increasingly demanding the higher the Prandtl number is. For this reason, first investigations of PAS have employed analytic approximations of the true flow field [16,23,24]. Later on, simulations of PAS based on flow field satisfying the Navier-Stokes equations have been carried out for low and moderate Prandtl numbers by several authors [14,15,17,25,26] with the highest Prandtl number $Pr = 28$ having been investigated numerically by Romanò and Kuhlmann [18].

To cope with problem 2 the above mentioned numerical investigations have all assumed a one-way coupling between particle and flow. This approximation is well established and reliable for dilute suspensions. In this approach, the influence of the particles on the fluid flow is neglected, as are mutual interactions among the particles. Typically, a sufficient number of noninteracting particles is initialized at random positions in a given flow, and the evolution of the particle ensemble is monitored as a function of time, where the particle transport in the bulk is modeled by the Maxey-Riley equation [27] or a variant thereof.

The bulk transport alone, however, is insufficient to explain the observation that small *neutrally buoyant* particles are attracted to PAS on a very short timescale (see [8], Fig. 14 of [10], and [28]). This indicates another aspect of problem 2: the necessary modification of the bulk-transport model when a finite-size particle moves near a boundary of the domain. A corresponding correction is most important for the motion near the free surface, because the thermocapillary stresses generate the

highest flow velocities on the free surface. Associated with the high surface velocity is a streamline crowding which is the reason why particles are frequently transported very close to the free surface. Despite its relevance for the problem at hand, the interaction of a finite-size particle with a flow boundary has never been fully resolved for the thermocapillary liquid bridge. Existing studies were concerned only with simpler settings such as, for example, a particle settling on a wall in a quiescent fluid under the action of gravity [29,30], or the motion of a particle near an interface between two immiscible viscous fluids in simple shear flow [31]. Perhaps the most relevant investigation, in the current context, regarding the motion of a particle near a free surface subject to shear is due to Romanò and Kuhlmann [32]. They numerically calculated the particle motion in an open two-dimensional cavity whose free surface is subject to a constant shear. In their two-dimensional computations all relevant temporal and spatial scales were resolved during the particle-boundary interaction. Comparing their fully resolved, albeit two-dimensional, results with those obtained by the simpler lump model of Hofmann and Kuhlmann [14], a very good agreement was obtained. This required, however, one to replace the particle size in the lump model by a suitably selected collision parameter which takes into account the width of the lubrication gap between the particle's surface and the interface. Other models for the motion of the particle near a moving boundary based on asymptotic solutions for the settling of a sphere near a wall or a free surface [33] have as well been suggested [34]. They essentially yield the same accumulation structures as predicted by the simpler model of Hofmann and Kuhlmann [14] and Romanò and Kuhlmann [32] and only slightly modify the dynamics. Therefore, the modified model of Romanò and Kuhlmann [32] based on the work of Hofmann and Kuhlmann [14] appears to be the most efficient and sufficiently accurate approach for predicting PAS to date.

To take into account the motion of the particles near the free surface, Hofmann and Kuhlmann [14] modeled the particle-surface interaction as an inelastic collision of the particle with the free surface when the spherical particle would touch the liquid-gas interface. Upon contact the normal component of the velocity of the particle is instantaneously annihilated. After sliding along the interface the particle would detach from the interface when it arrives at a point at which the normal velocity is directed inward and the particle resumes its motion in the bulk. Idealizing the motion of the particles in the bulk, Hofmann and Kuhlmann [14] were able to qualitatively explain the accumulation of particles along closed threads (PASs) as well as on tubular structures by means of a perturbed twist map.

The particle-surface interaction due to the finite size of the particle is key for PAS. It introduces a strong dissipation in the dynamical system describing the particle motion. In case of pure advection in the bulk, the particle-surface interaction is the only source of dissipation in the dynamical system. This is important to note, since dissipation is a necessary condition for the existence of attractors in dynamical systems [35]. Assuming finite-size particles are advected by a HTW for $Pr = 4$ in the bulk, Hofmann and Kuhlmann [14] discovered that the KAM structure of the HTW is a template for PAS. After repeated visits to the free surface many particles are transferred, by means of the particle-surface interaction, from chaotic to regular streamlines and keep moving on periodic or quasiperiodic orbits.

Hofmann and Kuhlmann's model [14] improved by Romanò and Kuhlmann [32] has been successfully tested by comparison with experiments on the particle motion in steady axisymmetric thermocapillary flows [36]. Using the improved model, key experimental results on PAS in liquid bridges with $Pr = 28$ [9,12,37] were reproduced numerically by Romanò and Kuhlmann [18].

Recently Romanò *et al.* [38] demonstrated that PAS in liquid bridges is just a prominent example of a more general class of *finite-size coherent structures* (FSCSs). They pointed out that PAS is distinct from *inertial* Lagrangian coherent structures (LCSs), which rely on particle inertia [39,40]. A very detailed experimental study on periodic and quasiperiodic particle attractors, corresponding to FSCSs, in a lid-driven cavity is due to Wu *et al.* [41]. Several other boundary-driven cavity flows are characterized by regular streamlines which can serve as a template for FSCSs [42–46]. A review on all PAS- and FSCS-related literature was recently given by Romanò and Kuhlmann [47].

While for small density-matched particles the mechanism of PASs and FSCSs is independent of particle inertia and buoyancy, buoyancy forces may prevent PAS for larger particles. For that reason experiments under weightlessness conditions are of interest and can be realized within the joint Japan-European Research Experiment on Marangoni Instability (JEREMI) which is planned for the International Space Station (ISS) [48]. While PAS has been studied extensively in low- and moderate-Prandtl-number liquid bridges on the ground, comprehensive experimental data and numerical results for Pr = 68, which is foreseen for JEREMI, are still lacking. Merely, a few hints about the existence of PAS in Pr = 68 thermocapillary liquid bridges have been detected during ISS experiments [49], while recent numerical studies [50,51] reported some preliminary findings on PAS formation. In the present study, we investigate PAS in thermocapillary liquid bridges for Pr = 68 to provide a numerical basis for future space experiments as well as to identify flow parameters and particle sizes for which PAS and FSCS are expected under zero gravity.

Section II presents the mathematical formulation of the problem. The numerical methods employed for simulating the flow and the particles are described in Sec. III. The general spatial structure of the hydrothermal wave for Pr = 68 is discussed in Sec. IV A, while the flow topology is analyzed in Sec. IV B. Results for PAS are provided in Sec. IV C. A summary of the results is given and conclusions are drawn in Sec. V.

II. PROBLEM FORMULATION

We consider a dilute suspension of small rigid spherical particles in a liquid bridge. The particle motion is predicted based on the one-way-coupling approximation [14,52] in which the effect of the particles on the flow field is neglected. This enables one to calculate the flow field beforehand, independent of the particles. The motion of each single particle in the given flow is then computed based on the forces acting on the particle.

A. Fluid flow

A liquid bridge made of an incompressible Newtonian liquid (density ρ_f, kinematic viscosity ν, thermal diffusivity κ) is formed in the gap of width d between two coaxial circular cylindrical rods of equal radius R. The aspect ratio is defined as $\Gamma = d/R$. The liquid bridge is held in place by the surface tension between the liquid and the surrounding gas.

The two support rods are kept at different constant temperatures $T_{\text{cold}} = T_0$ and $T_{\text{hot}} = T_0 + \Delta T$ with $\Delta T > 0$ being the temperature difference. As a result the surface tension between the liquid and the ambient gas varies and is approximated up to linear order by

$$\sigma(T) = \sigma_0 - \gamma(T - T_0), \tag{1}$$

where $\sigma_0 = \sigma(T_0)$ is the surface tension at the reference temperature and $\gamma = -\partial\sigma/\partial T|_{T=T_0} > 0$ is the negative surface-tension coefficient. The variation of the surface tension is usually very small compared to its reference value σ_0. This allows one to consider the asymptotic limit of vanishing capillary number $\text{Ca} = \gamma \Delta T/\sigma_0 \to 0$ in which the capillary pressure dominates the hydrostatic and the dynamic pressure. In this limit and for a liquid volume $V = \pi R^2 d$ the liquid bridge is cylindrical (Fig. 1).

While the surface tension variation (1) does not affect the shape of the liquid bridge for $\text{Ca} \to 0$, it causes tangential shear stresses, which act on the interface via the thermocapillary effect, thereby resulting in a thermocapillary flow. Under zero-gravity conditions buoyancy forces in the bulk are absent and the flow is driven only by thermocapillary surface forces.

The velocity and temperature fields in the cylindrical flow domain are obtained as solutions of the Navier-Stokes, continuity, and energy equations. Assuming constant material properties and using the thermal-diffusive scaling with d, κ/d, d^2/κ, and $\rho_f \kappa^2/d^2$ for length, velocity, time, and
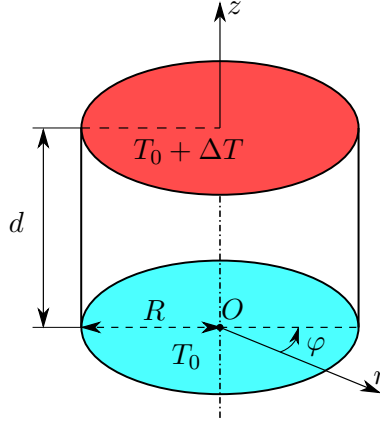
FIG. 1. Sketch of a liquid bridge with cylindrical shape. The hot and cold solid supports are indicated by color.

pressure, respectively, the governing equations are

$$(\partial_t + \boldsymbol{u} \cdot \nabla)\boldsymbol{u} = -\nabla p + \mathrm{Pr}\nabla^2\boldsymbol{u}, \tag{2a}$$

$$\nabla \cdot \boldsymbol{u} = 0, \tag{2b}$$

$$(\partial_t + \boldsymbol{u} \cdot \nabla)\theta = \nabla^2\theta, \tag{2c}$$

where $\boldsymbol{u}(\boldsymbol{x}, t) = u\boldsymbol{e}_r + v\boldsymbol{e}_\varphi + w\boldsymbol{e}_z$, $p(\boldsymbol{x}, t)$, $\theta(\boldsymbol{x}, t) = (T - T_0)/\Delta T$ are the dimensionless velocity vector, pressure, and reduced temperature, respectively, and $\boldsymbol{x} = r\boldsymbol{e}_r + z\boldsymbol{e}_z$ is the position vector with the polar unit vectors $\boldsymbol{e}_r$, $\boldsymbol{e}_\varphi$, and $\boldsymbol{e}_z$. The Prandtl number $\mathrm{Pr} = \nu/\kappa = 68$ is fixed corresponding to 5 cSt silicone oil, the working fluid to be used in the JEREMI space experiment. The physical properties of the fluid according to the data sheet of Shin-Etsu [53] are summarized in Table I.

The mathematical problem is closed by enforcing no-slip and constant-temperature boundary conditions on the cold and hot rods

$$z = 0, 1: \quad \boldsymbol{u} = 0, \quad \theta = 0, 1. \tag{3}$$

The velocity field on the free surface must satisfy no-penetration and thermocapillary stress conditions, while the viscous stresses from the gas phase are neglected. Furthermore, we assume adiabatic conditions, yielding

$$r = 1/\Gamma: \quad \boldsymbol{u} \cdot \boldsymbol{e}_r = 0, \quad \boldsymbol{e}_r \cdot \mathcal{S} \cdot \boldsymbol{e}_z = -\mathrm{RePr}\frac{\partial\theta}{\partial z}, \quad \boldsymbol{e}_r \cdot \mathcal{S} \cdot \boldsymbol{e}_\varphi = -\frac{\mathrm{RePr}}{r}\frac{\partial\theta}{\partial\varphi}, \quad \frac{\partial\theta}{\partial r} = 0, \tag{4}$$

where $\mathcal{S} = \nabla\boldsymbol{u} + (\nabla\boldsymbol{u})^{\mathrm{T}}$ is the viscous stress tensor in the liquid and

$$\mathrm{Re} = \frac{\gamma\Delta T d}{\rho_f \nu^2}, \tag{5}$$

TABLE I. Physical properties of 5 cSt Shin-Etsu silicone oil at 25 °C [53].

ρ_f [kg/m^3]	ν [m^2/s]	κ [m^2/s]	σ_0 [N/m]	γ [N/mK]
912	5×10^{-6}	7.353×10^{-8}	19.7×10^{-3}	6.37×10^{-5}

the thermocapillary Reynolds number. Instead of the thermocapillary Reynolds number Re, the Marangoni number Ma = RePr may be used.

Along with the Prandtl number, the fluid flow is determined by Γ and Re. Due to the computational cost associated with high-resolution numerical simulations necessary for resolving particle accumulation structures, we focus on Pr = 68 and the aspect ratio $\Gamma = 1$, considering Re = 1500, 1750, 2000, 2250, and 2500.

B. Fluid trajectories

When the Reynolds number exceeds a critical value Re_c the steady axisymmetric basic flow becomes unstable, for Pr $\gtrsim 1$, to a pair of azimuthally traveling three-dimensional waves, called hydrothermal waves (HTWs) [54,55]. Depending on the Prandtl number and the thermal conditions either a laminar standing wave or a laminar three-dimensional traveling wave with constant amplitude evolves for Re > Re_c and $t \to \infty$ [56]. Consistent with the result of Leypoldt *et al.* [57] we find standing waves for Pr = 68 at slightly supercritical Reynolds numbers. However, for all high Reynolds numbers considered here, we find the flow in form of a traveling HTW (see Sec. III A).

Hofmann and Kuhlmann [14] showed that the structure of the streamlines, called Lagrangian topology, is key to understanding and predicting PAS for small particles. Therefore, the Lagrangian topology of the thermocapillary flow is paid particular attention. Since the Lagrangian topology of a three-dimensional time-dependent flow is difficult to analyze, we take advantage of the fact that all azimuthal spectral components of the flow field of a traveling HTW have the same azimuthal phase velocity Ω_{HTW} [56]. This property enables us to transform the traveling wave $\boldsymbol{u}(\boldsymbol{x}, t)$ from the laboratory frame of reference to a frame of reference rotating with the same angular velocity $\Omega = \Omega_{\text{HTW}}$ as the wave, so that the traveling HTW becomes steady in the rotating frame. The flow in the rotating frame of reference is obtained as $\boldsymbol{U}(\boldsymbol{x}) = \boldsymbol{u}(\boldsymbol{x}, t) - r\Omega_{\text{HTW}}\boldsymbol{e}_\varphi$. A single snapshot of $\boldsymbol{u}(\boldsymbol{x}, t)$ is sufficient to obtain the traveling HTW in the rotating frame, up to a phase factor which depends on the time $t = t_0$ at which the snapshot is taken.

The traveling HTW being steady, trajectories of fluid elements coincide with streamlines in the rotating frame of reference. Therefore, both types of lines are governed by the advection equation

$$\dot{\boldsymbol{X}} = \boldsymbol{U}[\boldsymbol{X}(t)], \tag{6}$$

where $\boldsymbol{X}(t)$ denotes the position of an infinitesimal fluid element at time t. Equation (6) is invariant under the transformation to a rotating frame of reference with constant rotation rate. To obtain the Lagrangian topology, (6) must be solved for as many as possible initial condition $\boldsymbol{X}(t = 0) = \boldsymbol{X}_0$, covering the volume occupied by the fluid.

The flow state in form of a *traveling* HTW is important, because PAS has been observed only for traveling waves, but not for standing waves. The steady flow in the rotating frame of a *traveling* HTW allows for closed streamlines and closed streamtubes which serve as organizing centers (or templates) for PAS [14,15]. The existence of such streamtubes for certain Reynolds numbers is guaranteed by the analogy between steady three-dimensional incompressible flows and Hamiltonian systems [21]. On the other hand, there does not exist a frame of reference in which a standing wave would become steady. We are also not aware of any theory which has established a Hamiltonian framework for incompressible three-dimensional time-dependent flows which could prove the existence of closed streamtubes in standing HTWs. The absence of invariant streamtubes in standing HTWs is probably the reason PAS has never been observed in standing HTWs.

C. Particle motion

In the present one-way coupling approach the motion of noninteracting particles is approximated by the simplified version of the Maxey-Riley (SMR) equation [27] in the form provided by Babiano

et al. [52]. Given the steady velocity field in the rotating frame of reference $U(x)$ the SMR equation in the frame of reference rotating with the angular velocity $\mathbf{\Omega}$ is [14]

$$\ddot{X} = \frac{1}{\varrho + 1/2}\left[-\frac{\mathrm{Pr}}{\mathrm{St}}(\dot{X} - U) + \frac{3}{2}\frac{DU}{Dt} \right]$$
$$- 2\mathbf{\Omega} \times \left(\dot{X} - \frac{3}{2\varrho + 1}U \right) - \mathbf{\Omega} \times (\mathbf{\Omega} \times X)\left(1 - \frac{3}{2\varrho + 1} \right), \tag{7}$$

where X denotes the nondimensional position vector of the particle centroid and D/Dt is the material derivative following the flow. Two additional dimensionless numbers arise in the SMR equation (7): the particle-to-fluid density ratio ϱ and the Stokes number St defined as

$$\varrho = \frac{\rho_p}{\rho_f} \quad \text{and} \quad \mathrm{St} = \frac{2a_p^2}{9d^2}, \tag{8}$$

where a_p is the radius of the spherical particle and ρ_p its density. With definition (8) St is merely a quadratic measure of the particle size. Equation (7) yields a good approximation to the motion of a small particle if

1. the dimensionless radius of the particle $a = a_p/d \ll 1$ is small, $\rho\mathrm{St} \ll 1$,
2. the particle moves far away from the domain boundaries,
3. the particle Reynolds number $\mathrm{Re}_p = a|\dot{X} - U|/\mathrm{Pr} \ll 1$ is small, and
4. the suspension is dilute with a volume fraction of particles less than $O(10^{-3})$.

All conditions except for (2) hold true for the cases considered. Condition (2) cannot be satisfied, because the motion of the particle is hindered by its size near the boundaries of the flow domain, in particular near the free surface. Therefore, the modified particle-surface interaction (PSI) model of Hofmann and Kuhlmann [14] and Romanò and Kuhlmann [18] is employed. Since the particles planned to be used in the JEREMI space experiment and considered in this study are larger than $a_p \gtrsim 1\,\mu$m, Brownian motion is negligible [58]. Owing to condition (1), the Faxén correction can be neglected as it is proportional to a^2, so it represents a higher-order correction in terms of the Stokes number. In the case that the streamline curvature is significant, i.e., if $\nabla^2 u \gg 1$, the Faxén correction may be important. However, for the present thermocapillary flows the streamline curvature is significant only near the triple-phase contact lines at the hot and cold rods, where the PSI model is applied. Hence the effect of the Faxén correction is inherently embedded in the PSI model. Another term neglected by the SMR equation is the Saffman lift force, which represents an inertial correction to the Maxey-Riley equation. The Saffman lift tends to zero when the particle Reynolds number Re_p tends to zero [see condition (3)]. Finally, the Basset history term is neglected in the simplified Maxey-Riley equation because it is a higher-order correction in St. A quantitative criterion for estimating the importance of the Basset force was proposed by Coimbra and Rangel [59], who considered a Stokesian particle immersed in an oscillatory flow. They identified the parameter $S = a^2\hat{\Omega}/9\nu$, where $\hat{\Omega}$ is the forcing frequency of the relative particle velocity, and demonstrated that for $S \ll 1$ or $S \gg 1$ the Basset history force is negligible. In the present problem, the particle moves almost like the fluid and the frequency of closed streamlines in the rotating frame of reference near which PAS arises is very close to the frequency of the hydrothermal wave. Therefore, the forcing frequency experienced by the particle will almost be the frequency of the hydrothermal wave. With $\hat{\Omega} \approx \Omega_{\mathrm{HTW}} = O(10^3)$ ($m = 1$; see Table II below) and particles smaller than $a = 0.05$, one obtains $S = a^2\hat{\Omega}/9\nu \lesssim 5 \times 10^{-3} \ll 1$ and the Basset history force can be neglected. Moreover, as shown by Romanò *et al.* [34], the SMR equation is a consistent approximation when dealing with laminar bounded flows, since the added mass is more important than the Basset term in the bulk and both of them are much smaller than the particle-boundary interaction forces in the near-boundary region.

This inelastic collision model assumes that the particle centroid can approach the boundary up to some distance $\Delta = a + \delta$, comprising the dimensionless particle radius $a = a_\mathrm{p}/d$ plus a
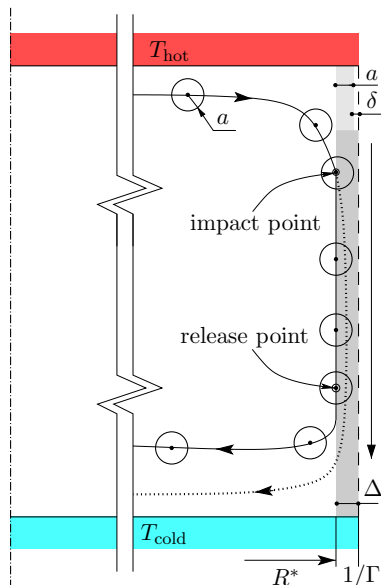
FIG. 2. Particle-boundary interaction modeled as an inelastic collision by the modified PSI model. The dotted line denotes the trajectory if a spherical particle of radius a would not see the boundary; the solid line represents the trajectory when the PSI model is enforced. Also indicated are the lubrication gap δ and interaction parameter $\Delta = a + \delta$.

dimensionless lubrication gap width δ (see Fig. 2). At this distance Δ (interaction parameter) from the flow boundary an approaching particle experiences an inelastic collision such that its velocity component normal to the boundary is annihilated. After the collision the particle centroid is supposed to slide, according to the z and φ components of (7), along a cylindrical surface with radius $R^* = 1/\Gamma - \Delta$, where $1/\Gamma$ is the dimensionless radius of the liquid bridge. The sliding continues as long as the flow velocity normal to the free surface at the location of the particle centroid is directed out of the liquid. As soon as the normal component of the velocity changes sign and turns inward, i.e., as soon as $U[(X(t)] \cdot n < 0$, where n is the outward normal vector, the particle is released back into the bulk, where it continues to satisfy (7).

For two-dimensional flows, Romanò and Kuhlmann [32] showed that numerical results obtained using the PSI model compare very well with fully resolved numerical simulations. Numerical calculations using the PSI model also compare well with experiments on axisymmetric flows [36]. Moreover, the PSI model including a properly selected lubrication-gap width δ, which may depend on a, ϱ, and the flow parameters, is capable of reproducing experimental PAS for Pr $= 28$ [18]. It is noteworthy that the PSI model acts directly on the particle velocity and does not require the inclusion of boundary-related forces in (7). Therefore, this approach has a conceptual advantage: different from force models, in which the particle motion near a boundary is affected by additional forces, e.g., lubrication forces defined by the asymptotic solution for the particle in the local Stokes flow [33,60], the PSI model can be combined with the perfect-tracer (advection) model (6) which does not include any dynamical-systems dissipation effect. The perfect-tracer model (6) is retrieved from (7) in the limit of St $\to 0$ and $\varrho \to 1$. Considering this limit allows one to prove that the particle accumulation obtained for this model derives solely from the particle-boundary interaction, since the PSI is the only source of dissipation in this framework. Furthermore, in the perfect-tracer limit, PAS exactly visualizes the relevant part of the Lagrangian topology.

III. NUMERICAL METHODS

A. Flow solver

The velocity and temperature fields are computed by solving numerically the governing equations (2) together with boundary conditions (3) and (4) for appropriate initial conditions $\boldsymbol{u}(\boldsymbol{x}, t = 0)$ and $\theta(\boldsymbol{x}, t = 0)$ on a very fine grid using the open-source software package OpenFOAM.

A standard pressure-based solver has been modified to include the thermocapillary stresses along the free surface. In order to smooth the singularities due to the discontinuous azimuthal vorticity at the three-phase contact lines at the hot and cold rods, a cosine regularization function $f(z)$ is introduced replacing the axial surface-stress condition in (4) by

$$\frac{\partial w}{\partial r} = -f(z)\mathrm{RePr}\frac{\partial \theta}{\partial z}, \quad f(z) = \begin{cases} \dfrac{1}{4}\Big[1 - \cos \dfrac{\pi z}{L}\Big]^2, & \text{if } z < L, \\[2mm] 1, & \text{if } L \leqslant z \leqslant 1 - L, \\[2mm] \dfrac{1}{4}\Big[1 - \cos \dfrac{\pi (1-z)}{L}\Big]^2, & \text{if } z > 1 - L, \end{cases} \tag{9}$$

where L is the length of the free-surface strip adjacent to the contact lines over which the boundary condition is smoothed. In test calculations [61] a regularization length $L = 0.02$ was found to be a good compromise between accuracy and required numerical effort. Therefore, this value is also used for the present calculations.

The numerical simulations are performed using a finite-volume solver on a collocated computational grid. For the pressure-velocity coupling the PISO (Pressure-Implicit with Splitting of Operators) algorithm with two external correction steps is selected. Two additional internal corrections are included to account for the nonorthogonality of the grid. The second-order central scheme and the implicit second-order backward scheme are applied for the spatial discretization and for the time integration, respectively. To solve the linear algebraic equations resulting from the pressure-projection step the preconditioned conjugate-gradient (PCG) method is used, while the linear equations resulting from the momentum and energy equations are solved iteratively using the preconditioned biconjugate gradient (PBiCG) method. For all dependent variables (pressure, velocity, and temperature) relative residuals less than 10^{-8} are reached at each time step before proceeding to the next time step.

The grid of finite-volume cells employed to simulate the flow for $\mathrm{Pr} = 68$ and $\Gamma = 1$ is shown in Fig. 3. During the calculations the mesh is refined in three steps from coarse to fine using 2 370 585 (coarse), 10 466 000 (medium), and 21 504 000 (fine) cells, where the mesh sizes are given excluding the boundary cells. Starting with the coarse mesh the simulation is advanced on each mesh until a fully developed periodic flow (fully developed HTW) is reached. Thereafter, the grid is refined using an interpolation consistent with the order of accuracy of the discretization scheme (second order) by employing the interpolant `mapFields` provided by OpenFOAM.

Using a small constant time-step of $\Delta t = 10^{-8}$ the equations are integrated until the flow becomes time-periodic. In all cases considered the periodic state is found to be a constant-amplitude *traveling* HTW. During each simulation the velocity and temperature are monitored at sixteen different points inside the liquid and on the free surface. When the traveling HTW is fully developed the signal at each monitoring point must be periodic with frequency F_{HTW} and suitable azimuthal phase relations must hold, depending on the fundamental azimuthal wave number m and the location of the probes. This yields the rotation rate of the wave $\Omega_{\mathrm{HTW}} = (2\pi/m)F_{\mathrm{HTW}}$. In the frame of reference rotating with the rotation rate Ω_{HTW} the HTW is stationary. This property is used to establish a convergence criterion. With F being the peak-to-peak frequency at time t of the periodic sinusoidal signal in the laboratory frame of reference, the flow field is transformed to a frame of reference rotating with the angular velocity $\Omega' = (2\pi/m)F$ at time t. The flow is assumed to have
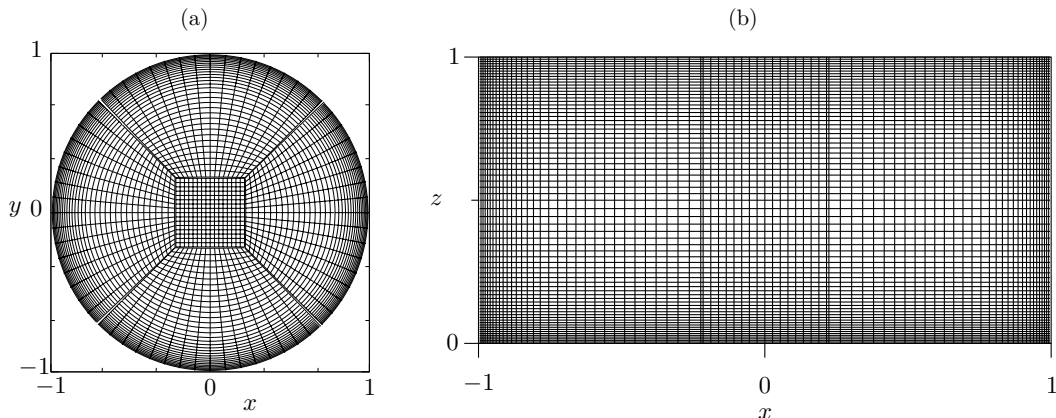
FIG. 3. Computational grid as seen in the horizontal (x, y) cross section (a) and in the vertical (x, z) plane (b). The grid employed for computing the Lagrangian flow topology is five times finer than the one depicted, consisting of 21 504 000 cells (excluding boundary cells). Double lines indicate the meshing blocks employed in `blockMesh` to define the computational grid.

become steady in this frame of reference when the condition

$$\max_{\bm{x},i} \frac{|u_i(\bm{x}, t) - u_i(\bm{x}, t - \Delta t)|}{\mathrm{RePr}\Delta t} \leqslant 10^{-5} \tag{10}$$

is satisfied at time t in the rotating reference frame. This termination criterion can hold only if the flow is almost constant in time in the frame of reference rotating with Ω'. The angular velocity Ω' at which the convergence criterion (10) is satisfied is then identified as the rotation rate of the traveling hydrothermal wave $\Omega_{\mathrm{HTW}} = \Omega'$.

The procedures described above as well as the regularization of the boundary conditions were tested and verified in Kuhlmann and Lemée [61]. For $\mathrm{Pr} = 28$, an excellent agreement was obtained between the numerical and experimentally measured angular frequencies of the hydrothermal waves [18].

B. Trajectories of fluid elements and of particles

Once the flow field has become steady, streamlines of the HTW in the rotating frame of reference are computed by numerically integrating the advection equation (6) using the Runge-Kutta Dormand-Prince method [62] for given initial positions $\bm{X}(t = 0) = \bm{X}_0$. This method employs standard fourth- and fifth-order Runge-Kutta schemes at each time step. An estimate of the numerical error is derived from the difference between the two results. Hereinafter, the absolute and relative errors estimated by the Dormand-Prince method are enforced to be less than 10^{-9} by adaptively selecting the time-step size Δt. For streamline integration the velocity field must be known at arbitrary points. This requires an interpolation of the discrete flow data which is accomplished by second-order interpolation, consistent with the accuracy of the flow solver.

Different from streamlines and tracer trajectories, particle trajectories are computed by solving the SMR equation (7) using a classical fourth-order Runge-Kutta method. To reduce the computational cost for the calculation of particle trajectories the steady velocity field $\bm{U}$ is interpolated (second order) from the OpenFOAM grid to a structured cylindrical grid. Another advantage of using cylindrical coordinates is that the cylindrical grid exactly fits the free surface of the liquid bridge and thus facilitates the implementation of the particle-surface interaction model. The cylindrical grid consists of $(N_r, N_\varphi, N_z) = (200, 240, 601)$ grid points, where N denotes the number of points per direction, yielding a total 28 848 000 grid points. To take care of the viscous and thermal

TABLE II. Angular phase velocity of the fully developed HTW as function of Re for $\mathrm{Pr} = 68$ and $\Gamma = 1$, given in the units of κ/d^2.

Re	$\Omega_{\mathrm{HTW}}\ [\kappa/d^2]$
1500	835.5
1750	901.2
2000	953.2
2250	988.8
2500	1026.6

boundary layers the cylindrical grid is compressed towards the support rods and the free-surface by the same amount as the original block-structured OpenFOAM grid.

To ensure an accurate integration of the SMR equation on the cylindrical grid, several tests have been performed. It was checked that regular streamlines obtained on an original block-structured grid are reproduced using the cylindrical grid, while streamlines initiated in the chaotic region are chaotic regardless of the grid used. Furthermore, for particles with $\mathrm{St} \lesssim 10^{-4}$ and $\varrho = 1$ the trajectories obtained integrating the SMR equation up to $t = 5$ on the cylindrical grid do not deviate by more than 10^{-3} from the streamlines computed on the original OpenFOAM grid. Since the computed HTW has a very small residual divergence error, tracer particles cannot accumulate by integrating the advection equation without taking into account the particle-surface interaction. This was verified using 4000 random initial conditions and integrating up to $t = 5$. The same was verified for the SMR equation, for the above parameters, using the same set of initial positions $\boldsymbol{X}(t = 0) = \boldsymbol{X}_0$ and initial velocities $\dot{\boldsymbol{X}}(t = 0) = \boldsymbol{U}(\boldsymbol{X}_0)$ matched to velocity of the flow. In particular, if a particle with $\varrho = 1$ and $\mathrm{St} = 10^{-5}$ is initialized velocity-matched on a regular streamline, it visibly stays on this streamline for at least up to $t = 5$ (the deviation of the trajectory from the streamline does not exceed 10^{-4}). From these tests we found a constant time-step size of $\Delta t = 10^{-7}$ to be sufficient for the desired accuracy if the SMR equation is integrated for no longer than $t = 5$ thermal-diffusive time units.

IV. RESULTS

A. Hydrothermal waves

A linear stability analysis for $\Gamma = 1$ reveals that the basic axisymmetric vortex flow considered here becomes unstable at a critical Reynolds number $\mathrm{Re}_c = 917$ [63]. The flow bifurcates, via a forward Hopf bifurcation, into a pair of counter propagating hydrothermal waves. Standing or traveling waves can arise. For adiabatic boundary conditions we find standing waves for slightly supercritical driving, whereas a constant-amplitude traveling wave is obtained for all higher Reynolds numbers considered herein, i.e., for $\mathrm{Re} = 1500, 1750, 2000, 2250$, and 2500. All traveling waves arise with a fundamental wave number $m = 1$ and propagate in the positive φ direction. The angular phase velocities of the HTWs are given in Table II.

Since the phase of the HTW in the rotating frame is arbitrary, depending on the instant at which the snapshot of the flow field is taken in the laboratory frame, we define the phase relative to the azimuthal angle at which the reduced temperature θ on the free-surface $r = 1/\Gamma$ in the midplane $z = 0.5$ reaches its maximum value $\theta_{\max}$. Thus

$$\theta_{\max} = \max_{\tilde{\varphi}} \theta(r = 1/\Gamma, \tilde{\varphi}, z = 0.5) = \theta(r = 1/\Gamma, \varphi := 0, z = 0.5), \tag{11}$$

where $\tilde{\varphi}$ is the original azimuthal coordinate which contains an arbitrary shift, and φ is the azimuthal coordinate relative to the angle $\tilde{\varphi}_{\theta_{\max}}$ at which $\theta = \theta_{\max}$. The temperature distribution on the free surface at midplane is shown in Fig. 4 for different Reynolds numbers. The hydrothermal wave becomes increasingly inharmonic and travels faster (Table II) the higher the Reynolds number is.
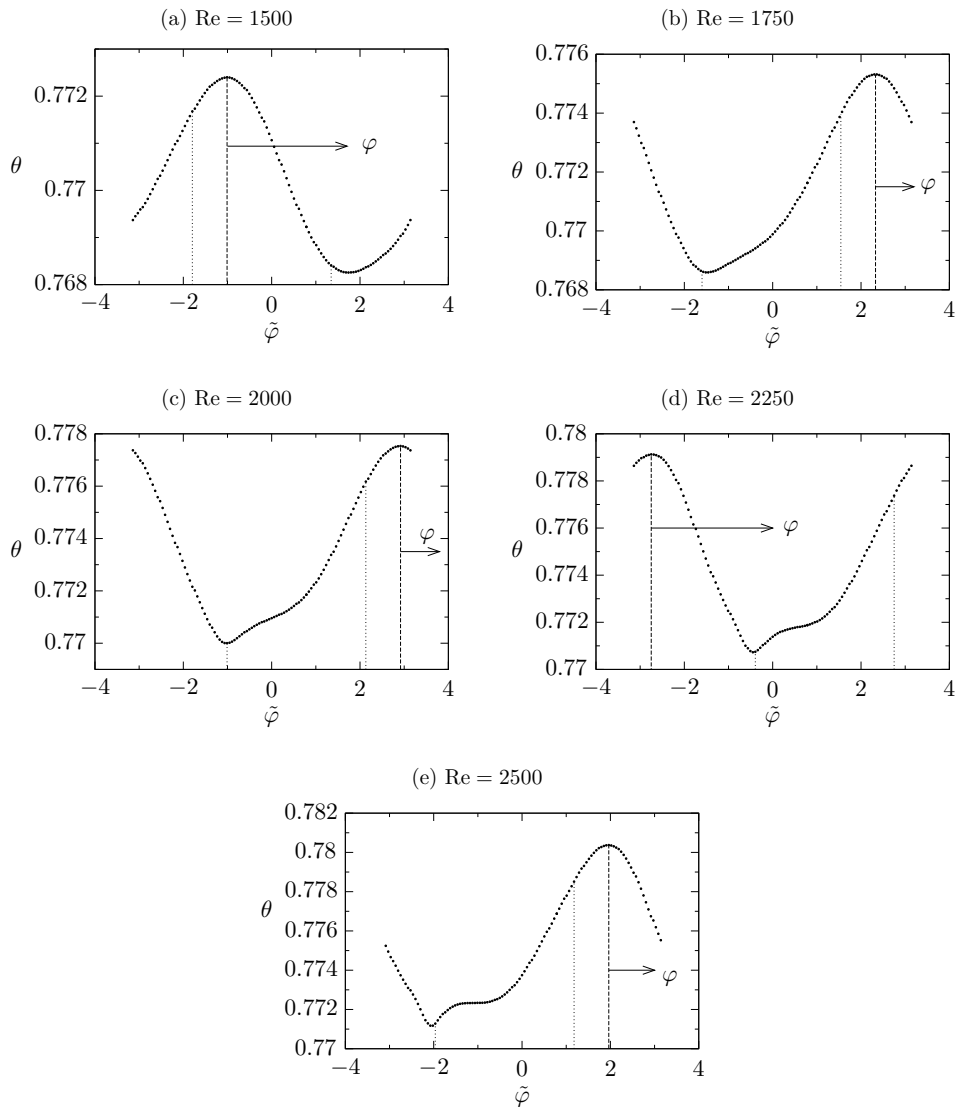
FIG. 4. Temperature distribution $\theta(r = 1/\Gamma, \tilde{\varphi}, z = 0.5)$ on the free surface in the midplane for $\Gamma = 1$. Here $\tilde{\varphi}$ is the phase angle in the rotating frame up to an arbitrary phase. The hydrothermal wave travels in the positive φ-direction shown by the arrow for all cases considered. The vertical dashed line indicates $\varphi = 0$. The vertical dotted lines indicate $\varphi = -\pi/4$ and $\varphi = 3\pi/4$ at which vertical cuts are taken below.

Note that the signature of the wave on the free surface at midplane is very weak, with peak-to-peak amplitudes less than 1% of the total temperature variation across the liquid bridge. The small surface temperature variation, as compared to a much larger temperature variation in the bulk, is a characteristic property of hydrothermal waves [54,64].

As a representative example, we discuss in some detail the flow fields of the HTW for $\Gamma = 1$ and the largest Reynolds number Re = 2500. The temperature field is shown in Fig. 5. Viewed from the hot wall in the negative z direction the wave propagating in positive φ direction appears to travel counterclockwise in the figure. Figures 5(a) and 5(b) show contours of θ in the midplane [Fig. 5(a)] and in a vertical cross section at $\varphi = -\pi/4, 3\pi/4$ [Fig. 5(b)]. The horizontal axis x'
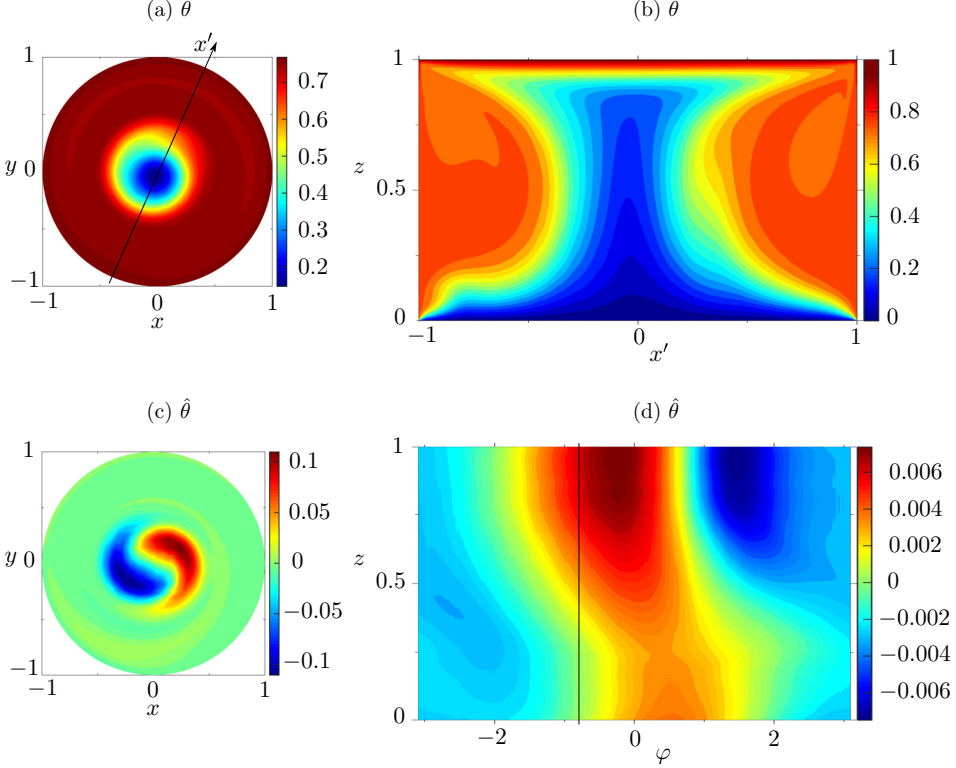
FIG. 5. Temperature field of a fully developed counterclockwise-traveling HTW for $\Gamma = 1$ and Re $= 2500$. The full temperature field θ is shown (a) in the midplane $z = 0.5$ and (b) in a vertical cross section at $\varphi = -\pi/4, 3\pi/4$. The nonaxisymmetric fluctuating part of the temperature field $\hat{\theta}$ is shown (c) in the midplane $z = 0.5$ and (d) on the cylindrical free surface $r = 1/\Gamma$. The vertical cross section at $\varphi = -\pi/4$ shown in (b) is indicated by the x'-axis in (a) and by the vertical black line in (d).

in the vertical plane $\varphi = -\pi/4$ is defined such that $\boldsymbol{e}_{x'} = \cos(\tilde{\varphi}_{\theta_{\max}} - \pi/4)\boldsymbol{e}_x + \sin(\tilde{\varphi}_{\theta_{\max}} - \pi/4)\boldsymbol{e}_y$. It can be seen that the temperature field is primarily determined by the basic axisymmetric flow. The toroidal vortex can be anticipated from Fig. 5(b) by the two large hot patches shown in a reddish color ($\theta \approx 0.75$). Cold fluid is transported towards the hot rod only along a slender region near the axis, where it undergoes rapid heating. As expected for such a large Marangoni number of Ma $= 1.7 \times 10^5$, the thermal boundary layers due to the strong convective effect are very thin on the hot and cold walls [Fig. 5(b)] and, in particular, near the hot and cold corners.

The fluctuating part of the temperature field of the hydrothermal wave $\hat{\theta} = \theta - (2\pi)^{-1} \int_0^{2\pi} \theta \, d\varphi$ is given by the deviation form the azimuthal mean. It is shown in the midplane [Fig. 5(c)] and on the free surface [Fig. 5(d)]. From Fig. 5(c) it is noticed that the fluctuations have the largest amplitude in the interior of the liquid bridge with an amplitude in the midplane of about 10%. The weak hot and cold filaments of the temperature fluctuations extend axially and split azimuthally (not shown) as they approach the hot wall, where they leave their signature on the free surface in form of very weak hot and cold spots with amplitude of ≈ 0.006 (note the scale) near the hot wall [Fig. 5(d)]. The inharmonicity in φ of the wave is clearly seen. The wave fronts on the free surface are slanted with respect to the z direction giving the impression as if the wave also propagates towards the hot wall in a certain region near $z = 0.5$.
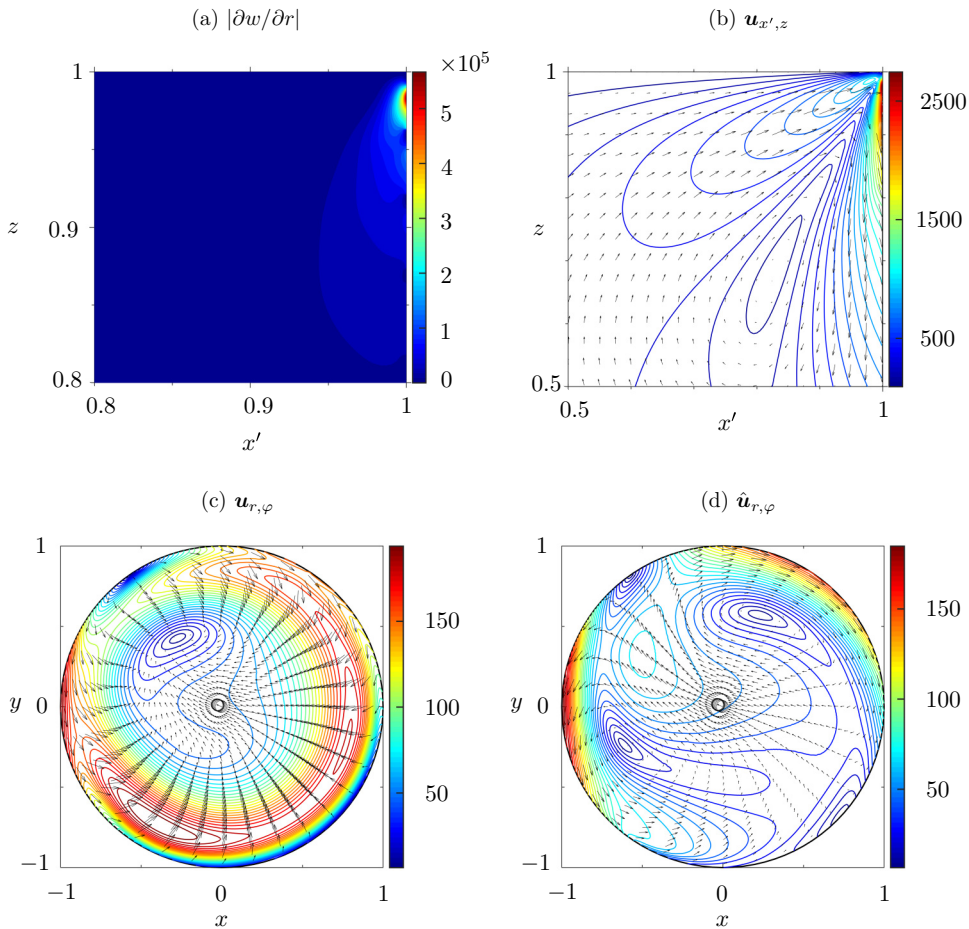
(a) $|\partial w/\partial r|$

(b) $\boldsymbol{u}_{x',z}$

(c) $\boldsymbol{u}_{r,\varphi}$

(d) $\hat{\boldsymbol{u}}_{r,\varphi}$

FIG. 6. Velocity field of a fully developed counterclockwise-traveling HTW for $\Gamma = 1$ and Re $= 2500$ in the laboratory frame of reference. (a) Magnitude of the axial shear stress $|\partial w/\partial r|$ in the plane $\varphi = -\pi/4$. (b), (c) Velocity vectors (arrows) and velocity magnitude (isolines in color) near the hot corner in the plane $\varphi = -\pi/4$ (b) and in the midplane $z = 0.5$ (c). (d) Velocity vectors (arrows) and velocity magnitude (isolines in color) of the fluctuating part of the velocity field in the midplane.

The largest surface-temperature gradients arise near the hot corner and create a thermocapillary stress primarily acting in the negative z direction. The resulting large radial gradient of the axial velocity near the hot corner is illustrated in Fig. 6(a) by showing $|\partial w/\partial r|$ in the (x', z) plane. The axial shear $|\partial w/\partial r|$ [Fig. 6(a)] attains its largest value on the free surface near the hot corner. Defining the projection of the velocity field onto the vertical plane (x', z) as $\boldsymbol{u}_{x',z} = (\boldsymbol{u} \cdot \boldsymbol{e}_{x'})\boldsymbol{e}_{x'} + w\boldsymbol{e}_z$, its magnitude and direction near the hot corner are shown in Fig. 6(b) by color and arrows, respectively. As a result of the thermocapillary stresses, the fluid is attracted from the bulk [arrows in Fig. 6(b)] to the hot corner and ejected mainly axially along the free surface. The fluid is also attracted from the free surface to the cold corner, but to a much lesser degree, since the region of high axial shear stress near the cold corner arises over a much smaller distance from the cold corner. Therefore, the toroidal vortex flow covers the whole length of the liquid bridge with the highest velocities arising in the upper part of the liquid bridge, in particular, near the hot corner. We did not find any flow separation from the solid walls as was observed in buoyant thermocapillary flow for Pr $= 28$ and $\Gamma = 0.68$ [18].

The projection of the velocity field onto the midplane $z = 0.5$, defined as $\boldsymbol{u}_{r,\varphi} = u\boldsymbol{e}_r + v\boldsymbol{e}_\varphi$, is shown in Fig. 6(c). The flow is seen to be strongly asymmetric with cross flow at the origin, characteristic for a HTW with $m = 1$. The nonaxisymmetric (fluctuating) part of the flow in the midplane, defined as $\hat{\boldsymbol{u}}_{r,\varphi} = [u - (2\pi)^{-1} \int_0^{2\pi} u\, d\varphi]\boldsymbol{e}_r + [v - (2\pi)^{-1} \int_0^{2\pi} v\, d\varphi]\boldsymbol{e}_\varphi$, is shown in Fig. 6(d). It arises in form of two weak (compared to the axisymmetric part of the flow) vortices in the bulk which are driven by the weak azimuthal temperature gradients (stresses) on the free surface [see Fig. 5(d)]. The stronger fluctuating temperature extrema in the bulk [Fig. 5(c)] are created by the action of the weak perturbation vortices on the large radial temperature gradients shown in Fig. 5(b).

The axisymmetric part of the flow has closed streamlines and can be derived from a streamfunction. These streamlines are all regular, since the streamfunction plays the role of a Hamiltonian of the corresponding one-degree-of-freedom dynamical system, for which chaotic streamlines cannot arise [20]. As we shall see in the next section, the weak mainly axial vortices created by the fluctuations due to the HTW are sufficient to make almost all streamlines chaotic.

B. Streamline topology

The fully developed hydrothermal wave satisfying the convergence criterion (10) is stationary in the rotating frame of reference. Such an incompressible flow is equivalent to a piecewise Hamiltonian system with one and a half degrees of freedom [21] in which the velocity represents the flux in the phase space of the system. Therefore, both regular and chaotic streamlines can coexist in the flow. The closed KAM tubes are stationary in the rotating frame of reference and fluid is transported along the stationary tubes being confined to them. Therefore, the KAM tori can be considered closed material tubes. This property is preserved in the laboratory frame of reference. The tubes remain closed. Merely, the material tubes are no longer stationary, but spiral about the basic state vortex and the azimuthal transport in the tubes is due only to the weak azimuthal flow of the HTW. Therefore, fluid contained in these winding material tubes does not mix with the fluid outside of the tubes which moves on chaotic streamlines. Owing to the importance of regular streamlines for PAS [14–16], the streamline topology of the steady flow $\boldsymbol{U}(\boldsymbol{x})$ is analyzed in the rotating frame of reference with focus on the geometry of the KAM tori.

Regular and chaotic streamlines are, indeed, found to coexist for all Reynolds numbers considered. The high spatial resolution of the simulations enables one to identify various sets of KAM tori. In the center of each set of KAM tori there exists a closed streamline. It may wind several (n) times about the z axis before closing. To identify the closed streamlines we consider the Poincaré return map of different streamlines on the half-plane $\varphi = -\pi/4$. On this half-plane, a closed streamline of period n appears as a fixed point $\boldsymbol{x}'_*$ of the nth return to the half-plane. To find fixed points of period n we search for zeros of the vector function $\boldsymbol{f}(\boldsymbol{x}') = \boldsymbol{x}'_n(\boldsymbol{x}') - \boldsymbol{x}'$, where $\boldsymbol{x}'_n(\boldsymbol{x}')$ is the nth return to the Poincaré half-plane of the streamline initiated at $\boldsymbol{x}' = (x', z)$ in the same half-plane. The zeros $\boldsymbol{x}'_*$ of $\boldsymbol{f}$ are calculated by Newton-Raphson iteration with absolute accuracy of $\|\boldsymbol{x}'^{(k)} - \boldsymbol{x}'^{(k-1)}\| < 10^{-5}$, where k numbers the iteration step. The iteration uses initial conditions $\boldsymbol{x}' = (x', z) = (0.5 + 0.05 \times i, 0.1 + 0.05 \times j)$ on a regular grid in the Poincaré half-plane with $i = 0, 1, \ldots, 9$, $j = 0, 1, \ldots, 16$. To distinguish neutrally stable (elliptic) fixed points from unstable (hyperbolic) ones, a streamline is integrated from the obtained numerical approximation of the fixed point for as long as $t = 30$. If $\|\boldsymbol{x}'_{n \times i_n} - \boldsymbol{x}'_*\| < 10^{-5}$, i.e., almost zero, for all $i_n = 2, 3, \ldots$, the fixed point is classified as elliptic and the corresponding streamline is closed. Otherwise the fixed point is hyperbolic.

Once an elliptic closed streamline is found, surrounding KAM tori are obtained by computing streamlines originating from the close vicinity of the elliptic point. We define the largest reconstructible KAM torus as the torus obtained from the outermost regular streamline found near the closed streamline. The streamlines are classified either regular or chaotic according to at least 100 ordered returns to the Poincaré plane.
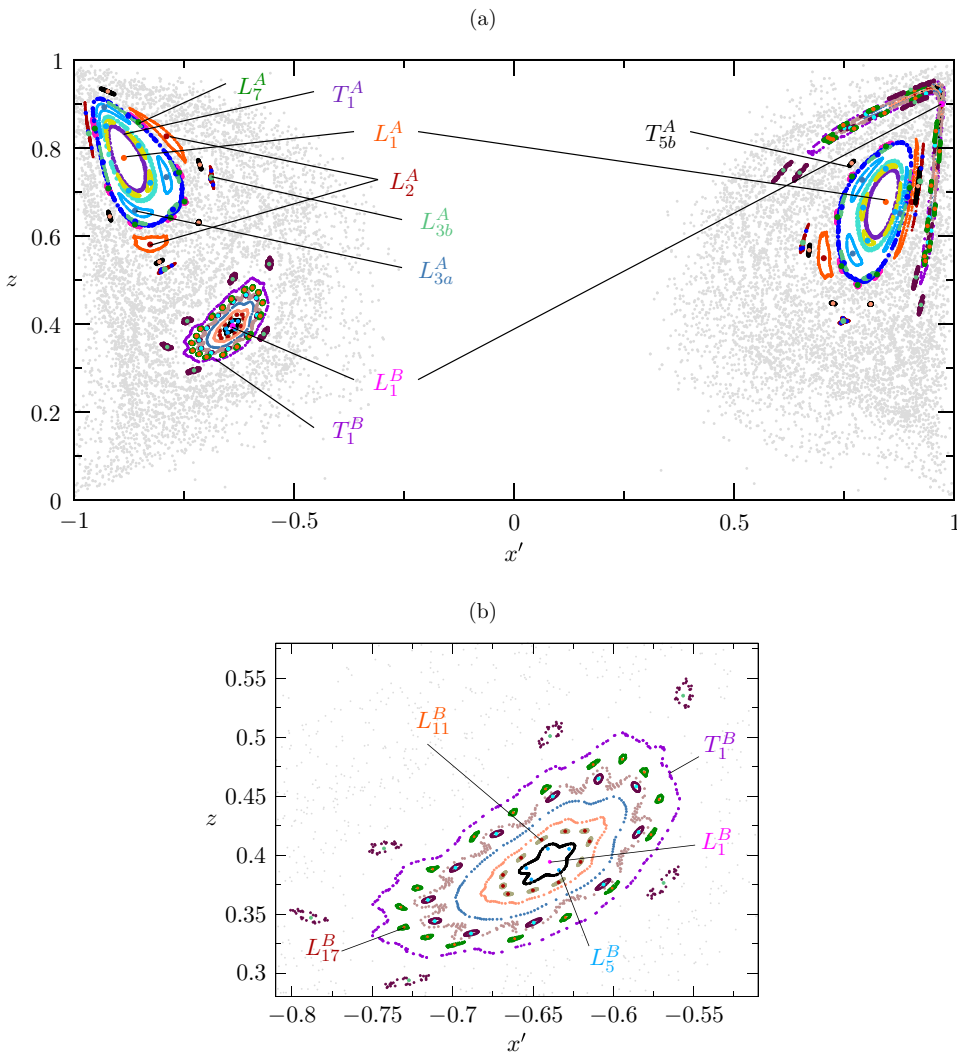
(a)

(b)

FIG. 7. (a) Poincaré section of streamlines in the (x', z)-plane ($\varphi = -\pi/4, 3\pi/4$) for $\Gamma = 1$ and Re = 1500. Gray (colored) Poincaré points indicate chaotic (regular) streamlines. Some of the closed streamlines (L) and KAM tori (T) are indicated by labels. (b) Zoom into the Poincaré section of the lower left group of KAM tori in (a).

As an example, the Poincaré section of streamlines on the full plane $\varphi = -\pi/4$ and $\varphi = 3\pi/4$ is shown in Fig. 7 for $\Gamma = 1$ and Re = 1500. To distinguish among the different structures, closed streamlines and KAM tori are denoted by L_n and T_n, respectively, where n is the azimuthal period of the object. Note that n can be larger than the fundamental azimuthal period $m = 1$ of the HTW due to the resonance phenomenon [65].

Two major groups of KAM tori, shown in color and indicated by superscripts A and B, can be identified in Fig. 7. Group A is organized around the closed streamline L_1^A, while group B is organized around L_1^B. Both closed streamlines wind once about the z-axis. In the bulk of the flow the KAM structures appear nicely ordered at $\varphi = 3\pi/4$ (left side of Fig. 7 with $x' < 0$). The streamline L_1^A does not approach any boundary closer than 0.1, neither in the Poincaré plane nor in the whole flow domain. This property suggests that small particles may not form PAS near L_1^A. On the other hand, L_1^B approaches the free surface much closer, and the whole group B of KAM tori becomes
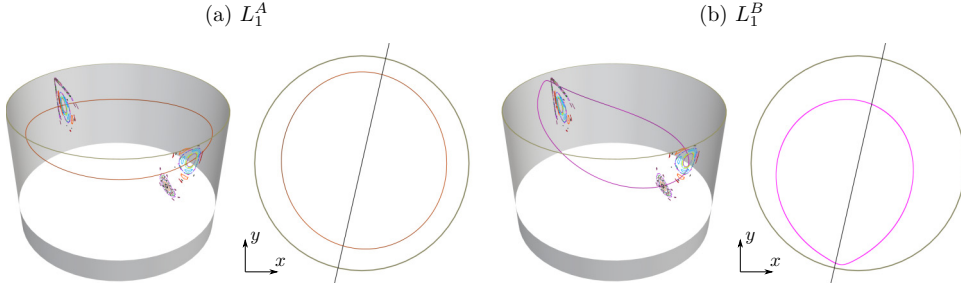
FIG. 8. Two central closed streamlines L_1^A (a) and L_1^B (b) for $\Gamma = 1$ and Re = 1500 which wind once about the axis. Left side of each subfigure: three-dimensional view of the closed streamline and Poincaré section. Right side of each subfigure: axial projection of the closed streamline with the location of the Poincaré plane (x' axis) indicated by the straight black line.

extremely squeezed and stretched near the free surface at $\varphi = -\pi/4$ (right side of Fig. 7 with $x' > 0$). Obviously, the stretching is caused by the high strain rates [see Fig. 6(a)] exhibited by the flow field due to the large thermocapillary stresses near the hot corner. Furthermore, the KAM tori of group B appear also wrapped around group A at $\varphi = -\pi/4$ ($x' > 0$). Based on the proximity of group B to the free surface, this group bears a potential for being important for PAS (see Sec. IV C).

Axial projections as well as three-dimensional views of the closed streamlines L_1^A and L_1^B are shown in Fig. 8 together with the Poincaré sections on $\varphi = -\pi/4, 3\pi/4$. The closed streamline L_1^B in Fig. 8(b) approaches the free surface relatively closely, up to a distance $\Delta_{FS} = 0.02794$. This is a hint at its potential importance for PAS when suitably sized particles are added to the liquid (see Sec. IV C). Many more complex closed streamlines exist. Examples are L_2^A, L_{3a}^A [Figs. 9(a) and 9(b)], and L_7^A [Fig. 12(a) below]. These streamlines are closed only after two, three, and seven revolutions about the axis, respectively. Note that a letter in the subscript distinguishes between different streamlines/KAM tori of the same azimuthal period that belong to the same group of KAM tori. A very intricate structure of the regular streamlines is found inside of the torus T_1^B [Fig. 7(b)]. This includes, among others, the closed streamlines L_5^B, L_{11}^B, and even L_{17}^B. According to the KAM theorem [65], these elliptic points are surrounded by KAM tori of the same period and alternate with hyperbolic fixed points which are embedded in chaotic layers. These examples illustrate the complex streamline structure of hydrothermal waves for Pr = 68.

To provide quantitative (reference) information on the flow topology for $\Gamma = 1$ characteristic data of the most prominent closed streamlines (L) and KAM tori (T) are gathered in Table III. Given in the table are the period of the closed streamline (τ) and the closest approach of the closed
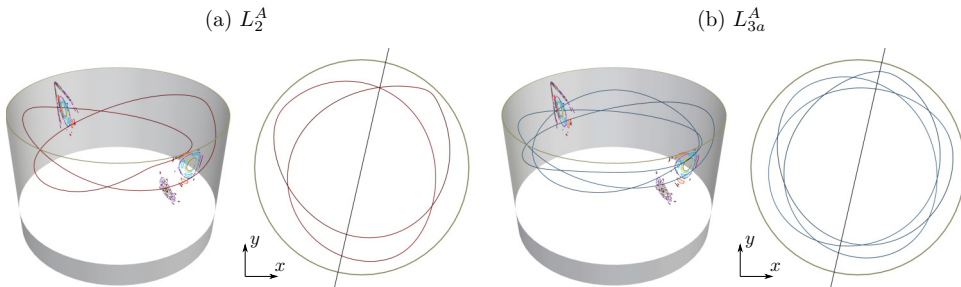

FIG. 9. Three-dimensional view (left) and axial projection (right) of closed streamlines L_2^A (a) and L_{3a}^A (b) for $\Gamma = 1$ and Re = 1500 which wind two and three times about the axis, respectively. Also shown is the Poincaré section (left) and the location of the Poincaré plane by the black line (right).

TABLE III. Characteristic data for some of the closed elliptic streamlines L and KAM tori T near which PAS is found. Given are the period τ of the closed streamline in the rotating frame and the minimum distances from the free surface (Δ_{FS}) and from the hot wall (Δ_W). The coordinates (x_0', z_0) in the plane $\varphi = -\pi/4$ define either a closed streamline or a streamline on the largest reconstructible KAM torus. The angle $\tilde{\varphi}_{\theta_{max}}$ characterizes the location of the plane $\varphi = 0$ with respect to the original computed flow field. Pr $= 68$ and $\Gamma = 1$.

Re	Streamline/KAM	τ	Δ_{FS}	Δ_W	(x_0', z_0)	$\tilde{\varphi}_{\theta_{max}}$
1500	L_1^B	0.00743	0.02794	0.06237	(0.97199, 0.89899)	-1.00980
	L_2^A	0.01506	0.03701	0.07743	(0.70366, 0.54863)	
	L_{3b}^A	0.02261	0.02507	0.05620	(0.92261, 0.72344)	
	L_5^B	0.03766	0.04525	0.09136	(0.96739, 0.92793)	
	L_7^A	0.05273	0.04103	0.08447	(0.74351, 0.53045)	
	L_9^A	0.06784	0.02423	0.05463	(0.91151, 0.64812)	
	L_{11b}^B	0.08191	0.02307	0.05323	(0.94816, 0.61140)	
	T_1^B		0.02278	0.05267	(0.93761, 0.52690)	
	T_{5b}^A		0.02737	0.06039	(0.72090, 0.44716)	
1750	L_1^B	0.00680	0.02707	0.06120	(0.96129, 0.77167)	2.32814
	L_9^B	0.06127	0.02455	0.05633	(0.94830, 0.62978)	
	T_1^B		0.02415	0.05554	(0.94085, 0.59982)	
	T_8^A		0.03969	0.08123	(0.81087, 0.49980)	
2000	L_1^A	0.00640	0.04141	0.08587	(0.88149, 0.61484)	2.91719
	L_1^B	0.00656	0.02578	0.05805	(0.96550, 0.75765)	
	L_4^B	0.02578	0.01948	0.04450	(0.96553, 0.66376)	
2250	L_1^B	0.00612	0.02838	0.06177	(0.96284, 0.72148)	-2.74889
	L_2^A	0.01262	0.03703	0.07541	(0.88799, 0.62966)	
	L_5^A	0.03163	0.02647	0.05520	(0.90777, 0.81681)	
	L_7^B	0.04298	0.02413	0.05212	(0.96688, 0.94472)	
2500	L_2^A	0.01219	0.02829	0.06335	(0.83488, 0.46749)	1.96349
	L_7^B	0.04129	0.01923	0.04585	(0.97857, 0.92628)	
	T_1^B		0.02388	0.05564	(0.94554, 0.56269)	

streamline/KAM torus to the free surface (Δ_{FS}) and to the hot wall (Δ_W). The cold wall is never approached as close as the hot wall. In addition, the locations of the closed streamlines are specified by providing the respective fixed points in the plane $\varphi = -\pi/4$. In case of a torus, we specify a point which defines the torus by the streamline originating from this point. Finally, we note the angle $\tilde{\varphi}_{\theta_{max}}$ by which the original coordinate system has to be rotated to satisfy (11). From Table III one can see that the closed streamlines and KAM tori are located much closer to the free surface than to the hot (or the cold) wall.

As the Reynolds number is increased, some regular regions of the flow persist, at least up to Re $= 2500$, the largest Reynolds number considered. However, the KAM tori have the tendency to become more slender. Figure 10 shows Poincaré sections for Re $= 1750$ and 2000, and Fig. 11 for Re $= 2250$ and 2500. For Re $= 1750$, 2000, and 2250 the main topological features of the flow are similar to the ones found for Re $= 1500$ with two groups of regular regions organized around L_1^A and L_1^B. The higher the Reynolds number the closer T_1^A approaches the free surface. Between Re $= 2000$ and 2250 L_1^A undergoes a period-doubling bifurcation and transforms into L_2^A [cf. Figs. 10(b) and 11(a)], still being surrounded in some distance by KAM tori of period one.
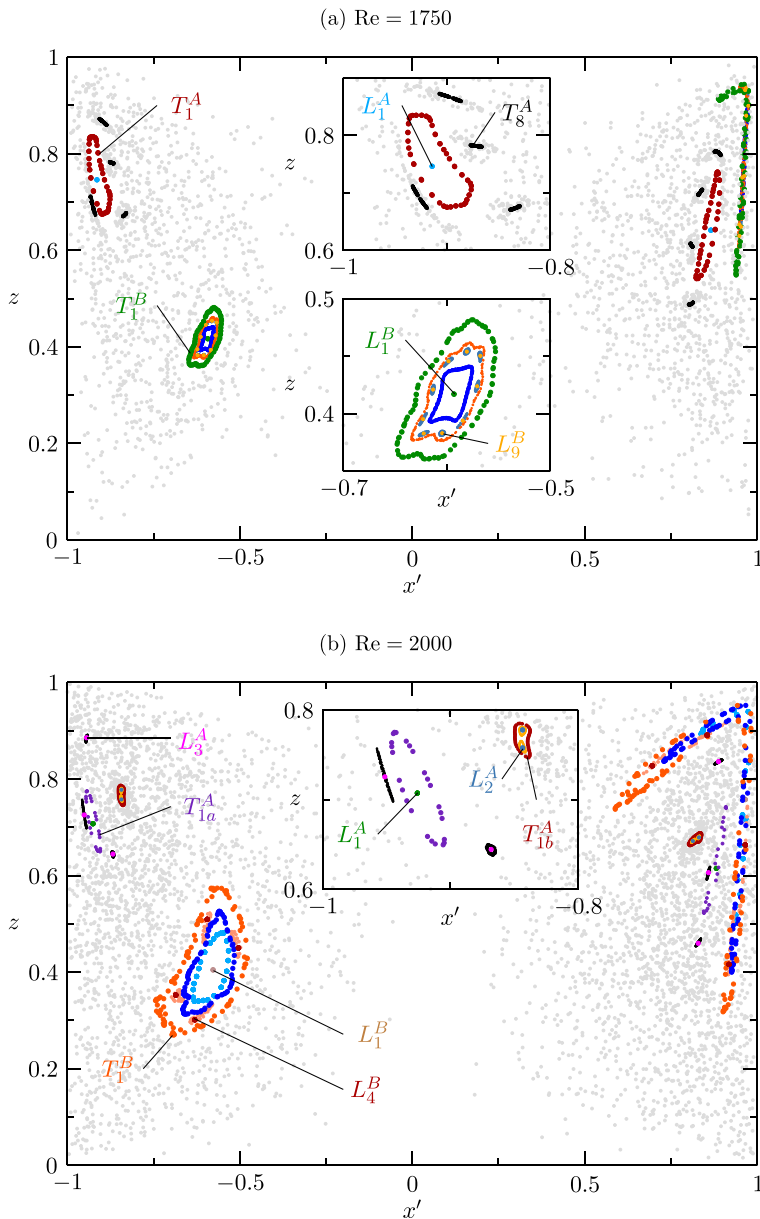
FIG. 10. Poincaré sections of streamlines in the (x', z)-plane ($\varphi = -\pi/4, 3\pi/4$) for $\Gamma = 1$: (a) Re = 1750, (b) Re = 2000. Gray (colored) Poincaré points indicate chaotic (regular) streamlines. Some of the closed streamlines (L) and KAM tori (T) are indicated by labels. Also shown are zooms into the Poincaré sections of the upper left (a, b) and lower left (a) groups of KAM tori.

Moreover, an additional regular region, which is encompassed by T_{1b}^A and contains L_2^A, is found near T_{1a}^A for Re = 2000 [Fig. 10(b)]. For Re = 2250 [Fig. 11(a)], the regular region which was surrounded by T_{1b}^A in Fig. 10(b) has become chaotic and no other regular region of period one is found in the vicinity of T_1^A anymore. At Re = 2500 the KAM tori of group A (T_1^A) have vanished and only the period-doubled tori [orange in Fig. 11(b)] around L_2^A have survived. On the other hand, T_1^B still exists at Re = 2500, although L_1^B has transformed into a closed streamline L_3^B with period three.
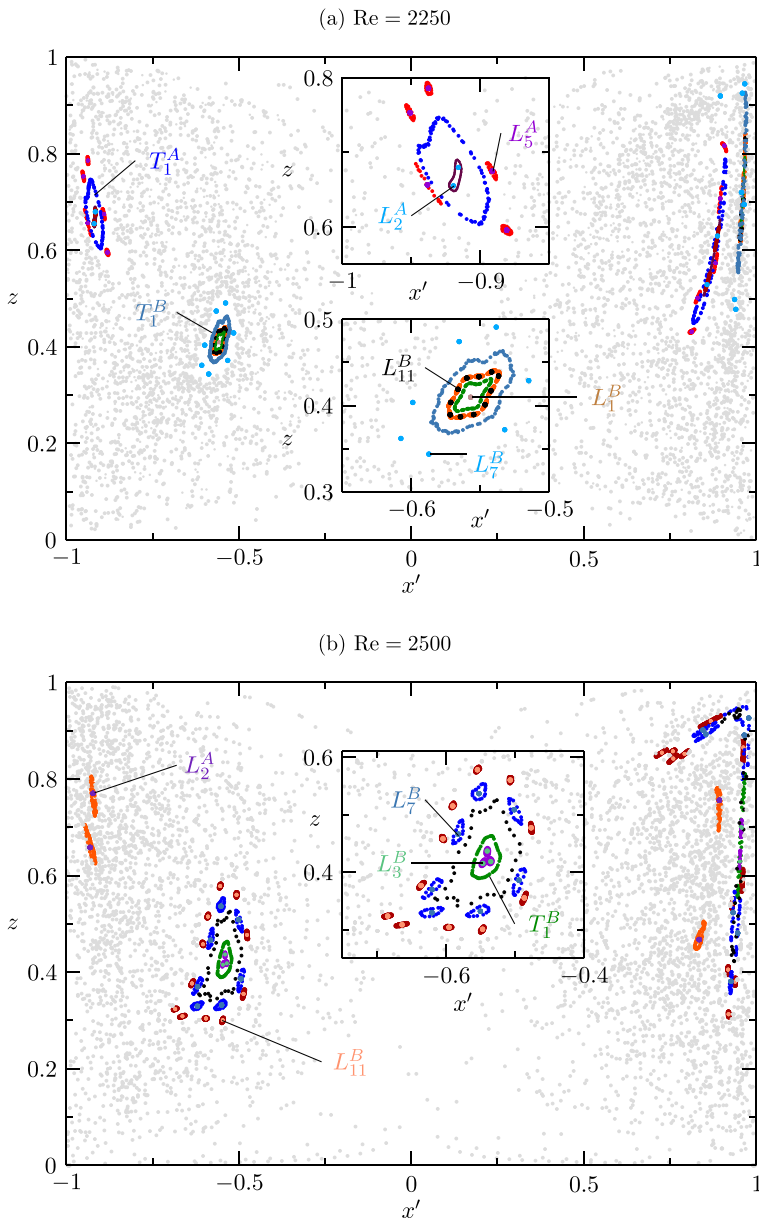
FIG. 11. Poincaré sections of streamlines in the (x', z)-plane ($\varphi = -\pi/4, 3\pi/4$) for $\Gamma = 1$: (a) Re = 2250, (b) Re = 2500. Gray (colored) Poincaré points indicate chaotic (regular) streamlines. Some of the closed streamlines (L) and KAM tori (T) are indicated by labels. Also shown are zooms into the Poincaré sections of the upper left (a) and lower left (a, b) groups of KAM tori.

For all Reynolds numbers considered, T_1^B is strongly drawn to the hot corner where the torus reaches the closest point of approach to the free surface, thereby being stretched the most in the axial direction. Therefore, the streamline topologies for all Reynolds numbers considered bear potential for PAS. Examples of closed streamlines for different Reynolds numbers are presented in Fig. 12. They are shown both in three-dimensional view along with the corresponding Poincaré section and in an axial projection as seen from the top (hot rod).

(a) Re $= 1500, L_7^A$

(b) Re $= 1750, L_1^B$

(c) Re $= 1750, T_8^A$

(d) Re $= 2000, L_1^A$

(e) Re $= 2000, L_4^B$

(f) Re $= 2250, L_5^A$

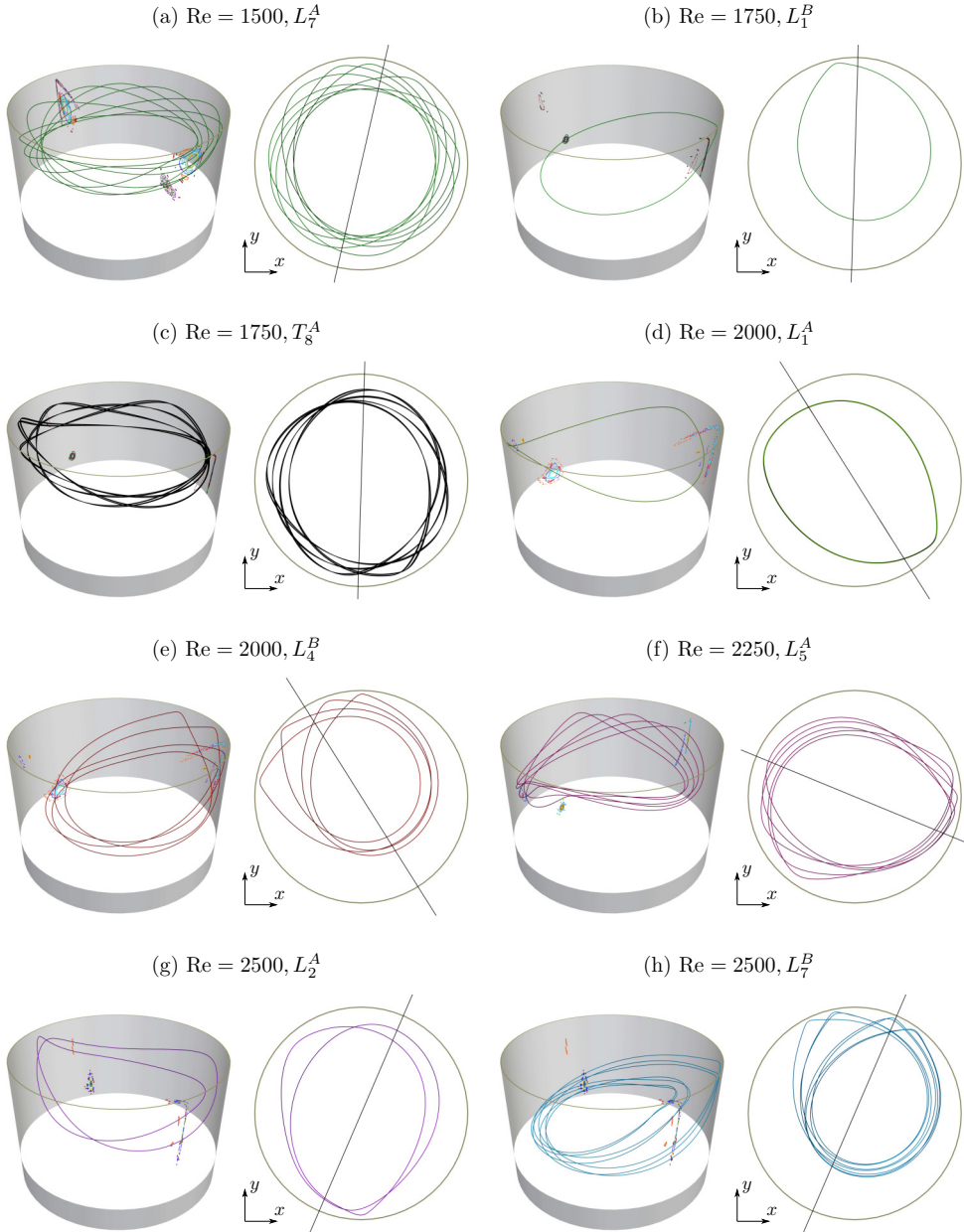(g) Re $= 2500, L_2^A$

(h) Re $= 2500, L_7^B$

FIG. 12. Three-dimensional view (left) and axial projection (right, view from the hot rod) of closed streamlines for different Reynolds numbers as indicated in the subcaptions. Also shown are the Poincaré section (left) and the location of the Poincaré plane (black line, right).

C. Particle accumulation structures

The motion of a particle depends on its relative density ϱ. An important limit is $\varrho = \rho_p/\rho_f \to 1$. Therefore, in a first step, we investigate PAS for small spherical particles which have the same density as the fluid, i.e., for $\varrho = 1$. Thereafter, the influence of a density mismatch $\varrho \neq 1$ on PAS is

considered as well as the alterations of the particle motion caused by changes of the flow field due to a change of the Reynolds number.

If density-matched particles are initiated velocity-matched to the flow, the SMR equation (7) reduces exactly to the advection equation (6). This also holds true if the modified particle-surface interaction (PSI) model [14,18] is implemented. The reason is the equivalence of (7) and (6) for velocity matching holds true component-wise and, after an interaction event, the particle is released to the flow with a vanishing boundary-normal velocity component. Therefore, the particle motion in the bulk of the liquid bridge can be obtained integrating (6), while near the free surface and the walls the modified PSI model is implemented. In this approach, the only parameter characterizing the particles is the thickness Δ of the layer on the boundaries (the free surface and the walls) which is not accessible by the centroids of the particles. Since the PAS obtained this way is formed solely due to the finite particle size, it represents a finite-size coherent structure (FSCS) [47].

1. Monitoring the temporal evolution of a particle ensemble

Within the present one-way coupling approach particle accumulation is a single-particle process. Nevertheless, it makes sense to consider an ensemble of noninteracting particles initialized at random positions, because the evolution of the ensemble takes into account the global attraction dynamics. For a quantitative characterization of the evolution of the ensemble we follow Muldoon and Kuhlmann [16] and introduce the same box counting measure $K(t)$ to quantify the accumulation process. To that end the liquid bridge is partitioned into N_{cells} cells of equal volume. For a given total number N of particles the accumulation measure

$$K(t) = \frac{1}{2(N - \bar{N})} \sum_{i=1}^{N_{\text{cells}}} |k_i(t) - \bar{N}| \quad (12)$$

with $K \in [0, 1]$ can then be defined as the normalized sum over all cells of the deviations of the number of particles $k_i(t)$ in each cell from the average number of particles per cell $\bar{N} = N/N_{\text{cells}}$. The same accumulation measure has already been used in numerical and experimental studies [50,66]. For convenience we select the number of cells $N = 4000$ equal to the number of particles, thus $\bar{N} = N/N_{\text{cells}} = 1$, and use $10 \times 40 \times 10$ cells in the radial, azimuthal, and axial directions, respectively. The widths of the cells in the azimuthal and axial directions are $\Delta\varphi = 2\pi/40$ and $\Delta z = (1 - 2\Delta)/10$, respectively. In order to satisfy the requirement of equal cell volumes, the radial cell length is $r_{i+1} - r_i = [(1/\Gamma - \Delta)^2/10 + r_i^2]^{1/2} - r_i, i = 1, \ldots, 10$.

2. PAS for density-matched particles

We consider the motion of 4000 noninteracting spherical particles governed by (6) and the PSI model. The particles are initialized at $t = 0$ at random positions within the volume accessible to the particle centroids. The large number of finite-size particles is merely used to improve the statistics, they do not interact with each other.

The evolution of the particle ensemble for $\Gamma = 1$ and Re $= 1500$ is shown in Fig. 13 for two different interaction parameters as it evolves from the random distribution shown in Fig. 13(a). To show the particle distribution within the liquid bridge we use the same coordinate system as for the flow streamlines presented above. Depending on the interaction parameter $\Delta = 0.037$ [Figs. 13(b)–13(d)] and $\Delta = 0.0082$ [Figs. 13(e)–13(h)] different PAS emerges. Particles which have undergone at least one interaction with the free surface or the solid walls are colored red, while particles which have not interacted with the boundaries up to the time displayed are colored blue. The time t which has passed since the initialization of the particle motion is given in Fig. 13 in units of the thermal diffusion time d^2/κ.

Graphs of the accumulation measure $K(t)$ for the evolution of the particle ensembles shown in Fig. 13 are presented in Fig. 14 (blue lines). The dashed red lines in Fig. 14 show the fraction N_{red}/N of particles which, at time t, have undergone at least one collision with the free surface, or, to be
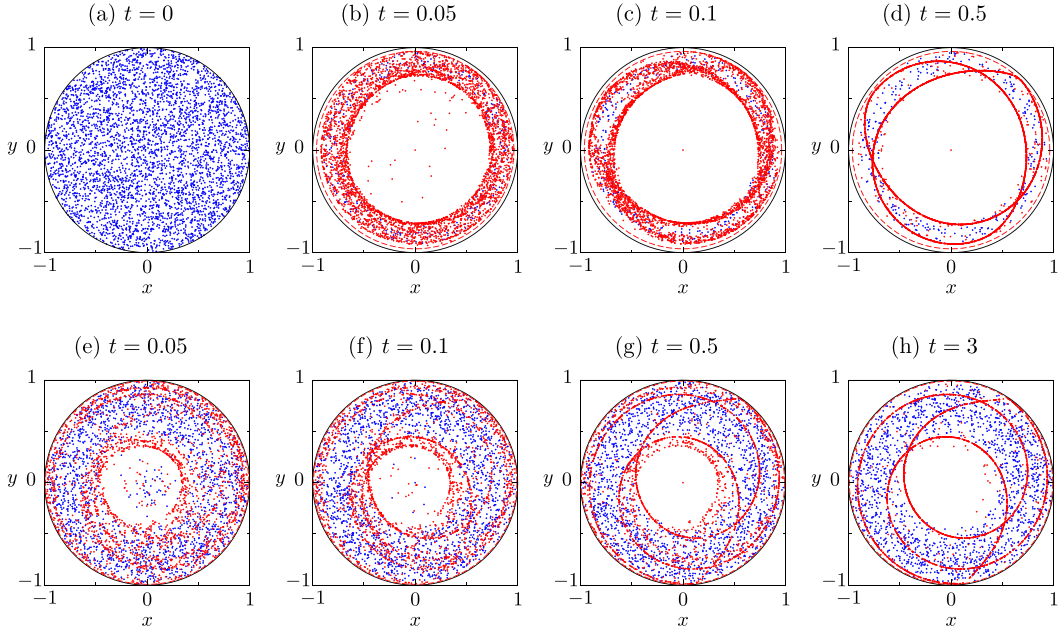
FIG. 13. Temporal evolution of the distribution of 4000 particles from random initial positions (a) for $\Gamma = 1$, Re = 1500, and $\Delta = 0.037$ (top row) and $\Delta = 0.0082$ (bottom row) shown in axial projection. Red dot: particle has undergone at least one PSI, blue dot: particle has not undergone any PSI. Time is indicated in the subcaptions. Note that the dot indicates the particle centroid, not the particle size. The dashed red circle of radius $R^* = 1/\Gamma - \Delta$ indicates the cylindrical surface on which the PSI occurs.

more precise, their centroid have visited the cylindrical surface of radius $R^* = 1/\Gamma - \Delta$ (illustrated by the dashed red circle in Fig. 13).

The particle-wall interactions arise mainly during the early phase of PAS evolution because of particles initialized near the axis of the liquid bridge and the solid walls. After the central and the wall regions of the liquid bridge have become depleted of particles, particle-wall collisions are very sparse, because the streamline crowding is most dense near the free surface.
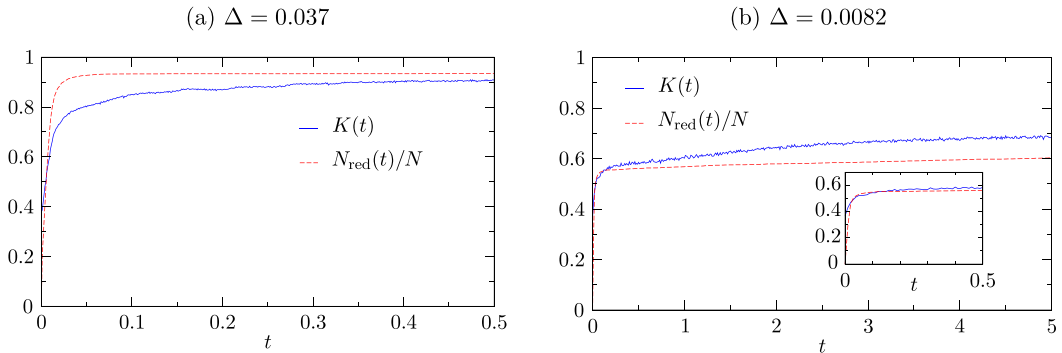

FIG. 14. Time evolution of the accumulation measure $K(t)$ (solid blue line) and of the fraction of particles N_{red}/N which have undergone a PSI at least once (dashed red line) for $\Delta = 0.037$ (a) and $\Delta = 0.0082$ (b). The parameters are the same as in Fig. 13.
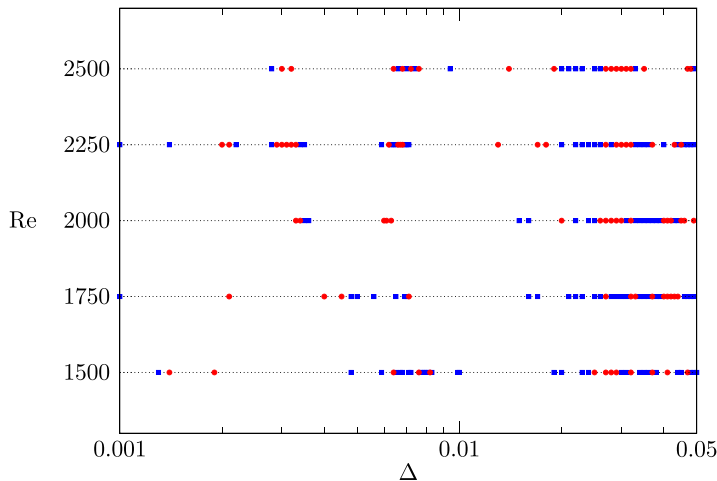
FIG. 15. Combinations of Δ and Re for which periodic (red dots) and quasiperiodic (blue squares) particle accumulation structures form by $t = 5$ in numerical simulations for $\Gamma = 1$ using advection in the bulk and the modified PSI model near the flow boundaries.

The initial random distribution with $K(t = 0, N \to \infty) = e^{-1} \approx 0.37$ rapidly increases to $K \approx 0.8$ within $t < 0.05$ indicating clustering. This is due to the fact that many particles from the region near the axis of the liquid bridge are directly advected to the free surface where they are removed from their streamlines by the first collision [67]. For the interaction length $\Delta = 0.037$, most particles (up to 90%) become colored red during this early phase of evolution. As a result of the PSI, the central region of the liquid bridge becomes rapidly depleted of particles [Figs. 13(b) and 14(a)]. The further gradual evolution of $K(t)$ to $K(t \to \infty) \approx 0.91$ is caused by the slower attraction of most of the particles ($\approx 93\%$ by time $t = 0.5$) to a periodic orbit by multiple PSIs. For the interaction length $\Delta = 0.037$ the periodic orbit which evolves practically coincides with the closed streamline L_2^A of the flow [compare Fig. 13(d) with Fig. 9(a)]. L_2^A is, in fact, tangent to a cylindrical surface of radius $R^* = 1/\Gamma - \Delta = 0.963$ at which the PSI takes place (see Table III for the closest approach of L_2^A to the free surface), so that most of the particles undergoing PSI are eventually released to T_2^A and cannot leave from there anymore [14].

Some particles ($\approx 7\%$ of all particles) never approach the free surface sufficiently close to undergo a PSI, since they have been initialized in KAM tori which are located further from the free surface than $\Delta = 0.037$. Therefore, these particles are always perfectly advected and will never be attracted to a limit cycle.

PAS can also form in the chaotic region [68]. This is found to be the case for smaller particles with the interaction parameter $\Delta = 0.0082$. The evolution of the particle ensemble is shown in Figs. 13(e)–13(h) and 14(b). The initial stage is similar to the one for larger particles discussed above, but only about 50% of the particles approach the free surface such that they experience PSI. They are depleted from the near-axis region, resulting in an accumulation measure slightly above 0.5 by $t = 0.05$. Further on, most particles are transferred by PSI to a trajectory which does not coincide with any closed streamline of the flow. Rather, particles gather on a limit cycle which is made of segments of two specific chaotic streamlines. Even though the underlying chaotic streamlines are open, the two streamline segments are closed by two PSIs on the free surface and after three revolutions about the axis [68]. Figure 13(g) shows the particle distribution at $t = 0.5$ is still diffuse in axial projection with slightly more than 60% of the particles having undergone at least one PSI and $K \approx 0.58$, while other particles are still moving in the chaotic toroidal core near the apparent vortex core of the flow. By $t = 5$ [Fig. 13(h)] PAS has become a sharp linelike structure [see also Fig. 16(e) in the next section], while more particles from the toroidal core continue to gradually
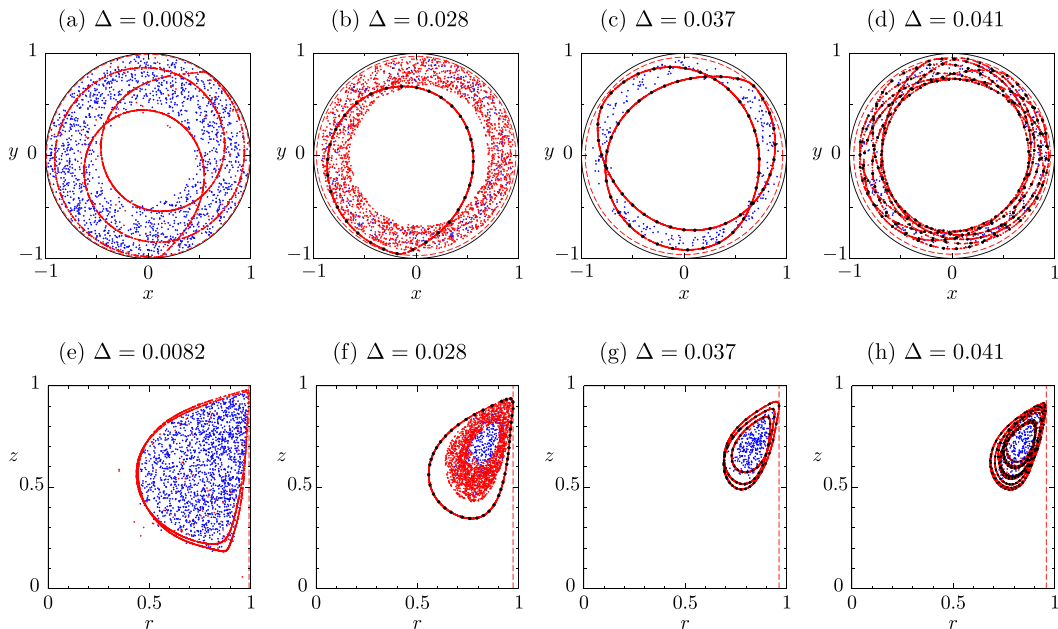
FIG. 16. Examples of PAS for $\varrho = 1$ in a thermocapillary liquid bridge for $\Gamma = 1$ and $Re = 1500$ at time $t = 5$. Shown are axial (top) and azimuthal (bottom) projections of the particle configuration for different values of Δ. Red dot: particle has undergone at least one PSI, blue dot: particle has never contacted the free surface. The cylindrical surface of radius $R^* = 1/\Gamma - \Delta$ is indicated by the dashed red circle (top) and by the dashed red straight line (bottom). Closed streamlines relevant for PAS are shown by dotted black lines in (b)–(d) and (f)–(h).

undergo their first PSI and accumulate on the periodic orbit. As can be seen from Fig. 14(b) this process is not very efficient and is characterized by a slow growth of K and N_{red}/N, also beyond $t = 5$. Conceptually, unless particles move in a distant KAM torus or in a distant separated chaotic region, all particles are expected to end up on the attractor for $t \to \infty$, because the chaotic sea of streamlines extends to the full free surface.

3. Existence range of PAS for density-matched particles

Owing to the complex structure of the KAM tori, particles can accumulate for a variety of particle radii. To obtain an overview on the parameters (Re, Δ) for which PAS forms the motion of 4000 initially randomly distributed particles with $\varrho = 1$ is computed up to $t = 5$ for each of the five Reynolds numbers considered and for interaction parameters densely covering $\Delta \in [0.001, 0.05]$ in steps of 0.001.

A particle ensemble qualifies as "PAS existing" if $K(t = 5) > 0.5$ and if the visual inspection indicates a periodic or quasiperiodic accumulation pattern. Periodic attractors appear sharp in axial and azimuthal projections of the particle positions, while a quasiperiodic structure appears diffuse. A quasiperiodic attractor, or tubular PAS (using the naming convention of Muldoon and Kuhlmann [16]), is expected to arise if $\Delta_{\text{FS}}(T) < \Delta$ and $\Delta_{\text{FS}}(L) > \Delta$ [14,16]. Such a quasiperiodic attractor can be clearly identified by Poincaré sections and distinguished from the quasiperiodic motion of noncolliding particles in distant KAM tori.

Parameters for which PAS exists according to the above-mentioned criterion are indicated in Fig. 15 by blue squares for quasiperiodic structures and by red dots for periodic structures or for cases when both periodic and quasiperiodic structures coexist. This does not mean that the time span of $t = 5$ is required for PAS to form. In fact, in many cases the particle accumulation occurs

on a shorter timescale. This can be seen from Figs. 13(d) and 14(a), where most of the particles cluster around the closed streamline L_2^A of the flow after $t = 0.5 \ll 5$. The largest probability for PAS for $\Gamma = 1$, as can be seen in Fig. 15, is found near $\Delta \approx 0.03$. Since $\Delta > a$ and usually $\Delta < 2a$ [18,32], the size of the spherical particles which qualify for PAS can be estimated as $a \in [0.015, 0.03]$. This corresponds to dimensional particle radii in the range $a_p \in [75, 150]$ μm for a liquid bridge with $d = R = 0.005$ m ($\Gamma = 1$). Accordingly, the dimensional time sufficient for PAS formation according to our criterion is $t = 5\,d^2/\kappa = 28.3$ min for a 5 cSt silicone oil with $\kappa = 7.353 \times 10^{-8}$ m^2/s.

4. Examples for particle accumulation

Figure 16 shows examples of PAS for $\Gamma = 1$ and Re = 1500 in axial and azimuthal projections for selected interaction parameters Δ at $t = 5$. The temporal evolution of the PAS shown in Figs. 16(a) and 16(e) ($\Delta = 0.0082$) and 16(c) and 16(g) ($\Delta = 0.037$) has been displayed before in Fig. 13. By comparing the PAS from Fig. 16 with the closed streamlines shown in Figs. 8, 9, and 12, it becomes evident that PAS preferentially forms very close to the regular streamlines that enter the narrow boundary layer of the thickness Δ on the free surface. The closed streamlines, indicated by dotted black lines, are indistinguishable from the red attractors on the scale of Fig. 16. The larger the interaction parameter Δ (larger particles), the more particles undergo interactions with the free surface and the more particles are depleted from the central region of the liquid bridge. In case of PAS these particles end up on periodic or quasiperiodic attractors [see, e.g., Figs. 16(b) and 16(f) and 16(d) and 16(h)].

The accumulation structures for $\Delta = 0.028$ shown in Figs. 16(b) and 16(f) are made of periodic, quasiperiodic, and strange attractors. For better identification we consider the last Poincaré point out of $t \in [0, 5]$ for each of the 4000 particles simulated. Poincaré sections are shown for two different azimuthal angles in Figs. 17(a) and 17(b). For $\varphi = -\pi/4$ [Fig. 17(a)] the streamline topology which has been presented before in Fig. 7 is shown in gray. In addition, a Poincaré section is shown for $\varphi = 2.0605$ [Fig. 17(b), with the horizontal axis denoted x'']. These azimuthal angles have been selected, because the PSIs leading to the attractors take place very close to these values of φ [Fig. 17(c)]. In Fig. 17 one can identify the periodic attractor (P, magenta) already visible in Figs. 16(b) and 16(f). The PSI leading to this attractor which is associated with the closed streamline L_1^B takes place near $\varphi = -\pi/4$ [Fig. 17(c)]. In addition, one can identify a quasiperiodic attractor QP_5 [black in Fig. 17, but red in Figs. 16(b) and 16(f)] which is created by PSIs at $\varphi \approx 2.18$–2.22 and which forms near the KAM torus T_{5b}^A (Fig. 7). As a third structure which is also created by PSI at $\varphi \approx 1.74$–2.07 one can identify a nearly quasiperiodic structure (red, related to the KAM structures of group A) which, however, is chaotic and can be termed *strange PAS* (S, red), according to the naming convention of Muldoon and Kuhlmann [16]. Particles cannot escape the strange PAS S due to the PSI. The PSIs for the quasiperiodic and the strange PAS arise in distinct regions of φ [Fig. 17(c)]. In addition to these structures, the Poincaré points of particles which have not undergone a PSI at $t = 5$ are shown in blue in Figs. 17(a) and 17(b). Most of these particles move inside of KAM tori of the flow. The remainder of the particles with blue Poincaré points may eventually be transferred to one of the accumulation structures for $t > 5$.

For smaller particles with $\Delta < 0.01$, for which the PSI occurs closer to the free surface than the closest approach of any regular streamline, particle clustering is still possible. An example is shown in Figs. 16(a) and 16(e). The periodic attractor arises along trajectories coinciding with (open) chaotic streamlines in the bulk which, however, are closed by the PSI near the free surface. This mechanism, also discussed in Sec. IV C 2, was first pointed out by Kuhlmann and Muldoon [68].

Even though the strain rate of the present flow is very high near the hot and the cold corner, test calculations for density-matched particles using (7) and an initial velocity mismatch of $\dot{X} = 2|U|\chi$, where the components of χ for each particle are assigned random numbers $\chi_i \in [0, 1]$, yielded essentially the same long-time behavior as for initial velocity matching in the presence of the PSI. This is interpreted as the particle-surface interaction being by far the strongest dissipative
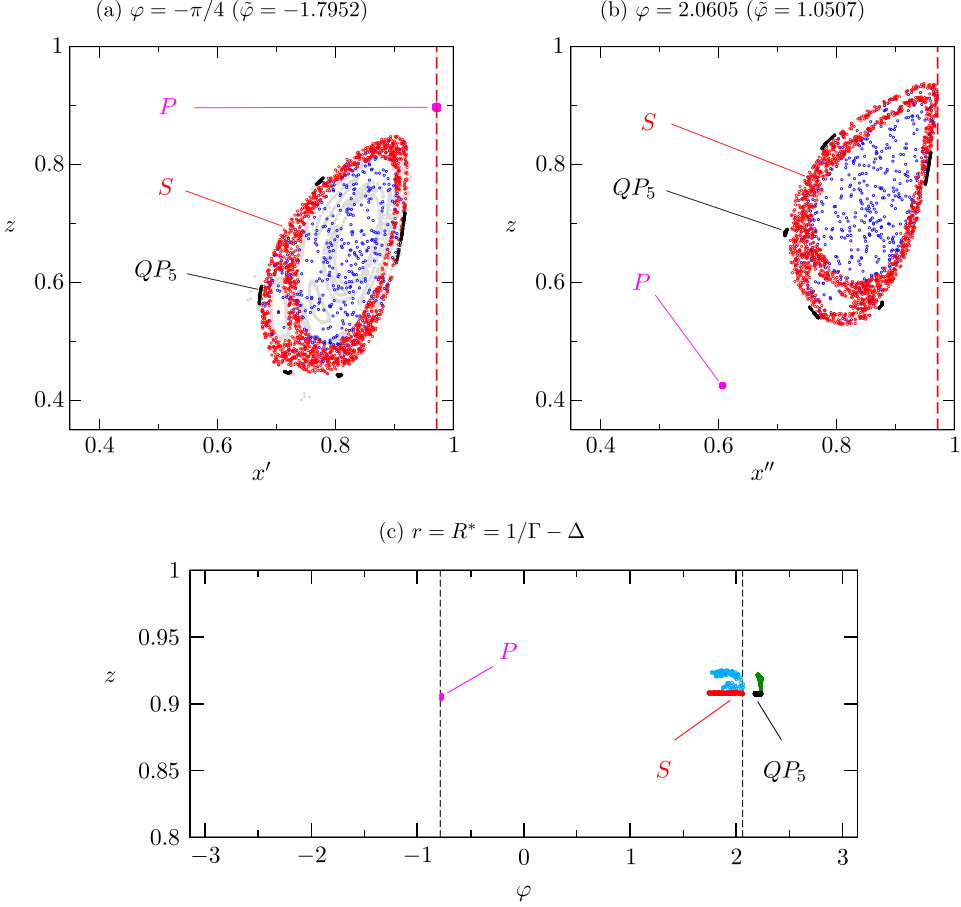
FIG. 17. Poincaré section of 4000 particle trajectories for Re = 1500 and $\Delta = 0.028$ showing only the last Poincaré point before $t = 5$ of each particle. Poincaré sections are shown at $\varphi = -\pi/4$ (a) and $\varphi = 2.0605$ (b). The colors indicate different accumulation structures (P: periodic, QP_5: quasiperiodic, S: strange) explained in the text. Blue dots indicate Poincaré points of particles not having experienced any PSI. The gray dots in (a) represent the Lagrangian topology [KAM tori of group A; cf. Fig. 7(a)]. (c) Collision points (green for QP_5 and bright blue for S) and release points [colors as in (a) and (b)] of particles on $r = R^* = 1/\Gamma - \Delta$ [dashed red lines in (a) and (b)]. The vertical dashed black lines in (c) correspond to the azimuthal angle φ of the Poincaré sections shown in (a) and (b).

mechanism and thus determining the attractors. This is in agreement with the results of Romanò and Kuhlmann [69].

5. Dependence of the particle accumulation on the density ratio

To investigate the alteration of PAS in the presence of mild inertia we consider the motion of particles whose density deviates from that of the fluid. To that end the relative density is varied in the range $\varrho \in [0.5, 2]$ and the SMR equation (7) is integrated for particles which are initiated with velocity matched to the velocity of the flow. Owing to the large parameter space we present results for the particle radius $a = 0.0185$ (St $= 7.606 \times 10^{-5}$). The particle motion is computed using the PSI model with $\Delta = 2a = 0.037$. This value for Δ is motivated by an order-of-magnitude estimate based on the results of Romanò and Kuhlmann [32] for very small particles.
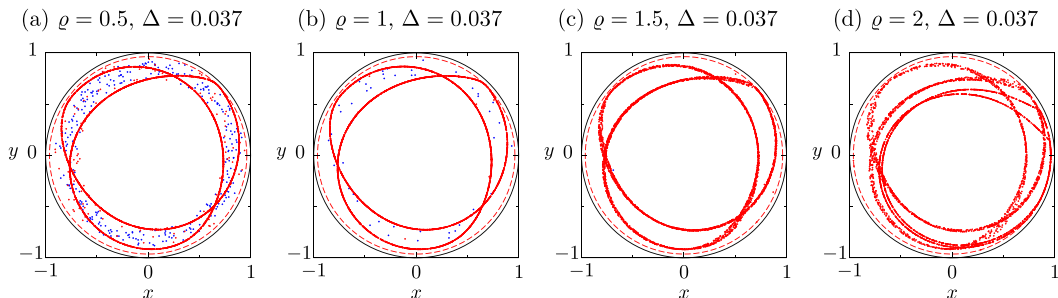
FIG. 18. Examples of PAS in a thermocapillary liquid bridge for $\Gamma = 1$, $Re = 1500$ and $a = \Delta/2 = 0.0185$ ($St = 7.606 \times 10^{-5}$) at $t = 1$. The particle density is indicated in the subcaptions. Lines, symbols, and colors as in Fig. 16.

Figure 18 shows results obtained for $\varrho = 0.5$ [Fig. 18(a)], 1 [Fig. 18(b)], 1.5 [Fig. 18(c)], and 2 [Fig. 18(d)]. In the presence of PSI (Fig. 18), we find PAS which does not deviate much from the PAS for density-matched particles [$\varrho = 1$, Fig. 18(b)]. The latter case has already been discussed above in Figs. 16(d) and 16(g): PAS forms near the closed streamline L_2^A which winds twice about the axis [Fig. 9(a)]. For light particles with $\varrho = 0.5$ [Fig. 18(a)] a similar line-like PAS forms near L_2^A, but with fewer particles having interacted with the free surface at $t = 1$. For heavy particles with $\varrho = 1.5$ [Fig. 18(c)] the particles cluster on a weakly quasiperiodic attractor QP_2 which, due to the particle inertia, appears slightly rotated from L_2^A in the clockwise direction in the reference frame rotating with the HTW, i.e., in the direction opposite to the sense of rotation of the HTW [compare Figs. 18(b) and 18(c)].

The toroidal nature of PAS QP_2 becomes even more evident in Fig. 19. The figure depicts the last intersection point within $t \in [0, 1]$ of each particle (black dot) with the half-plane $\varphi = -\pi/4$ [Fig. 19(a)] and with the half-plane $\varphi = 1.7498$ [Fig. 19(b)], in which the quasiperiodic attractor QP_2 for $\varrho = 1.5$ is nearly tangent to $r = R^*$ (indicated by a red dashed line). The horizontal axis is denoted x''. Figure 19(c) shows impact (green) and release (black) points of the PAS QP_2 on the cylindrical surface of radius R^* which intersects T_2^A (orange dots). The rotation of QP_2 with respect to the closed streamline L_2^A appears as a shift of the toroidal PAS relative to L_2^A in the Poincaré sections in Figs. 19(a) and 19(b).

For a particle twice as heavy as the fluid [$\varrho = 2$, Fig. 18(d)], particles gather at $t = 1$ near two different structures. One structure is sharply toroidal, appearing diffuse in the axial view. It is similar to QP_2 discussed above for particles with $\varrho = 1.5$ and forms as a toroidal structure rotated clockwise from L_2^A. The azimuthal shift with respect to the closed streamline increases as the density ratio ϱ (density mismatch) increases from 1.5 to 2. A similar azimuthal shift of pure inertia-induced limit cycles with respect to the closed streamline was found by Kuhlmann and Muldoon [24] (see Fig. 2 therein) for a similar flow.

The other attractor is periodic and arises near another KAM torus of period one (not shown), nested into T_1^B. The corresponding attracting orbit is closed after two revolutions about the axis. During each revolution of a particle on the periodic attractor one PSI takes place (two interactions per period of the closed orbit). This indicates that the new periodic attractor that arises for $\varrho = 2$ is also essentially caused by the PSI, while the inertia effect slightly modifies the particle trajectories in the bulk such that the PSI leads to an attracting orbit.

Computations for other particle sizes yield qualitatively similar results. Therefore, we conclude that not only density-matched particles can form FSCS. Also particle accumulation structures for light and heavy particles with $\varrho \in [0.5, 1.5]$ and $a \lesssim 0.02$ must be understood as FSCS, if the clustering mechanism is essentially due to the PSI. Of course, purely inertial clustering is possible, in principle, for weakly inertial particles near a closed streamline which is distant from the free surface. But the timescales on which such inertial structures form are usually orders of magnitude larger
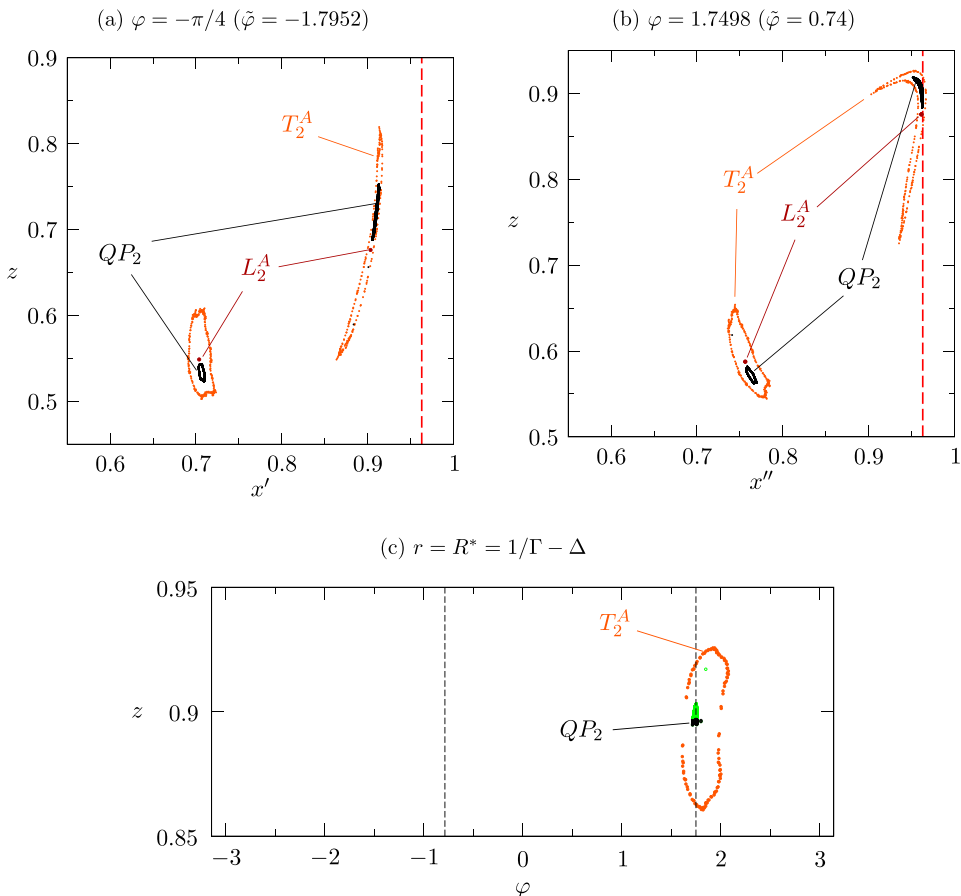
FIG. 19. (a), (b) Half-plane Poincaré section of the PAS for for $\Gamma = 1$, Re $= 1500$, $\varrho = 1.5$, $a = 0.0185$, and $\Delta = 0.037$ [Fig. 18(c)] showing the last intersection within $t \in [0, 1]$ of each particle simulated (black dots) superimposed on the Poincaré section of L_2^A (2 dark red dots) and T_2^A (orange dots). (c) Impact (green) and release (black) points of the PAS QP_2 with the cylindrical surface of radius $R^* = 1/\Gamma - \Delta$, indicated by the dashed red line in (a) and (b). The vertical dashed black lines correspond to φ of the Poincaré sections in (a) and (b).

than for FSCS [28,34]. For very small interaction lengths $\Delta < 0.001$ and particles with density larger than that of the fluid ($\varrho > 1$) we do not find periodic attractors. As might be expected, such particles are merely centrifuged out of the vortex of the basic flow, tend to approach the boundaries and may eventually come to rest on the solid walls.

6. Dependence on the Reynolds number

The existence and shape of PAS reflect the underlying KAM structure of the flow. For Pr $= 68$ and $\Gamma = 1$ the KAM template changes considerably with Reynolds number. Therefore, the type and existence of attractors for the particle motion are expected to vary with Re, even if Δ and a are kept constant.

Attractors due to PSI which are located in the chaotic region are found to be particularly sensitive to changes of the Reynolds number. For instance, PAS is observed at Re $= 1500$ for small particles with $\varrho = 1$ and $\Delta = 0.0082$, whereas accumulation is absent for higher Reynolds numbers. For
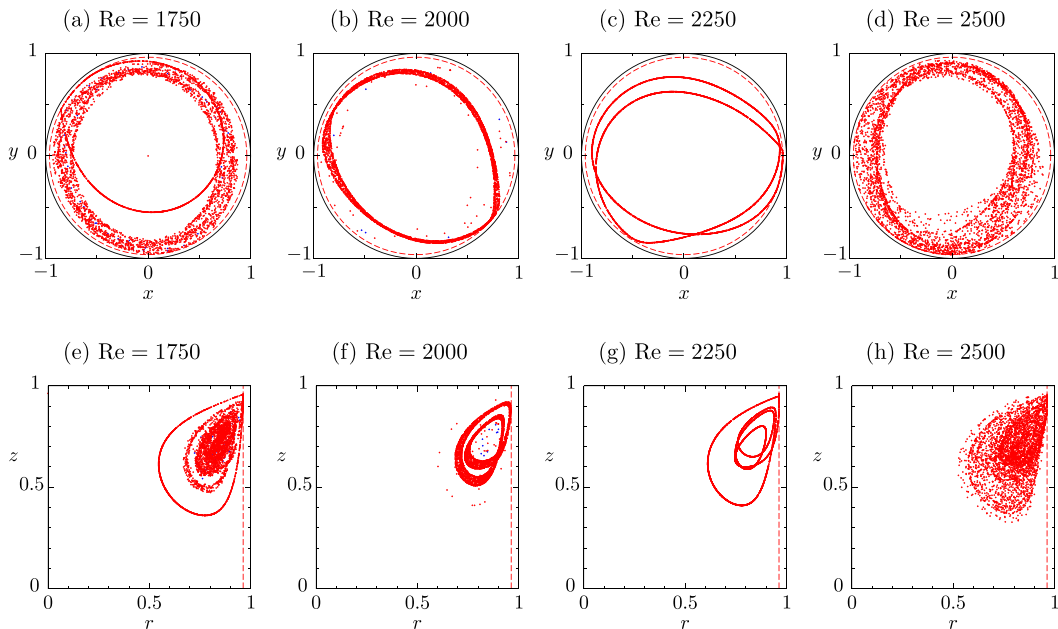
FIG. 20. Particle accumulation structures for $\varrho = 1$, $\Delta = 0.037$ and different values of Re as indicated. Shown are axial (top) and azimuthal (bottom) projections of the particle configuration at $t = 5$. Lines, symbols, and colors as in Fig. 16.

larger particles with $\Delta = 0.037$, on the other hand, PAS of different shapes is found, depending on Re. For Re $= 1750$ [Figs. 20(a) and 20(e)] particles accumulate both on a periodic and on a strange attractor, similar to the case of Re $= 1500$ and $\Delta = 0.028$ considered in Sec. IV C 4 [see discussion of Figs. 16(b) and 16(f) and 17]. In the bulk the periodic attractor is a streamline segment in the chaotic layer surrounding T_1^B, and it is closed near the free surface by one PSI after one revolution about the axis. Not all of the initially randomly distributed particles are attracted to this limit cycle. Most of the particles ($\approx 72\%$) cluster on a strange attractor in a chaotic layer in the vicinity of the KAM structures of group A, which they cannot escape due to PSI, while a small number of particles ($\approx 1\%$) initiated inside the KAM structures of group A never experience PSI and keep moving along the regular streamlines.

For the higher Reynolds number Re $= 2000$ and the same Δ, a quasiperiodic tubular PAS on a torus of T_1^A arises [Figs. 20(b) and 20(f)] for which the PSI takes place at an azimuthal angle rotated by about π with respect to the case of Re $= 1750$. Further increasing the Reynolds number to Re $= 2250$, a periodic PAS near L_2^A [Figs. 20(c) and 20(g)] is found. For even higher Reynolds number Re $= 2500$ and $\Delta = 0.037$ the particles do not find a periodic or quasiperiodic structure. Rather, they accumulate in a sharp torus-like region of period one near the hot corner and seem to move chaotically. The structure appears diffuse in the axial and azimuthal projections [Figs. 20(d) and 20(h)], as well as in the Poincaré section.

The higher the Reynolds number, the stronger is the streamline crowding near the free surface and the more particles undergo particle-surface interactions. For Re $= 1500$ and $\Delta = 0.037$, $\approx 7\%$ of all particles have never interacted with the free surface by $t = 5$. For Re $= 1750$ this number has reduced to $\approx 2\%$ [Figs. 20(a) and 20(e)], and for Re $= 2500$ all particles have undergone at least one PSI during this period of time [Figs. 20(d) and 20(h)]. As more streamlines of the flow enter the prohibited layer of thickness Δ on the free surface the stronger is the particle depletion effect in the bulk, in particular during the initial phase of evolution of the particle ensemble.
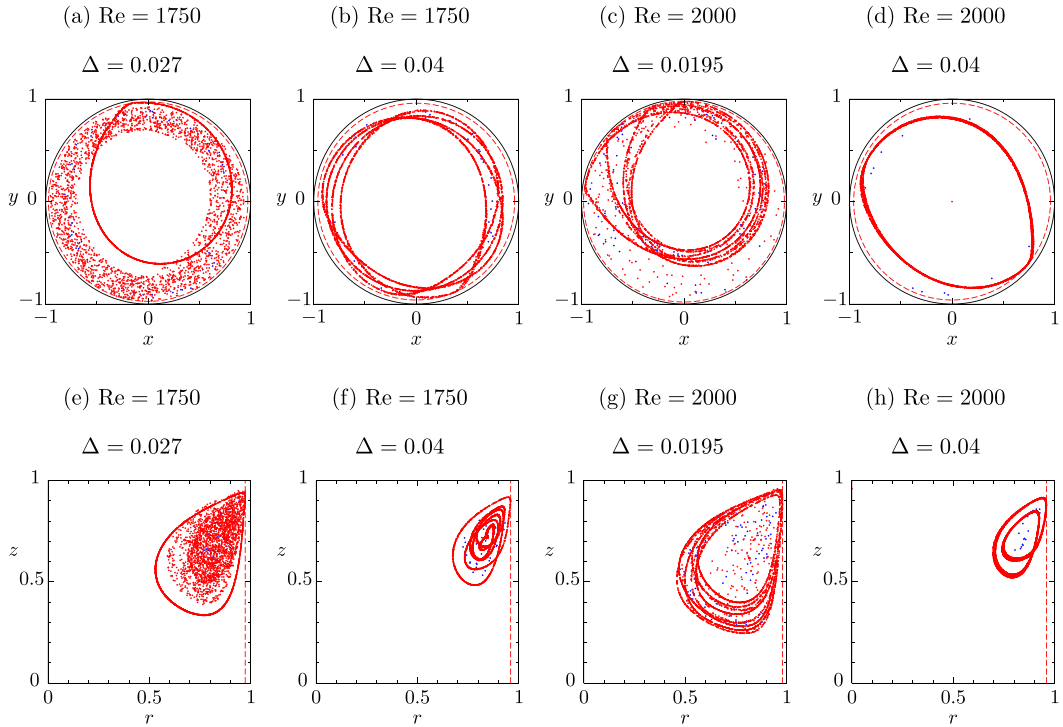
FIG. 21. Examples of PAS in a thermocapillary liquid bridge for $\Gamma = 1$ and Re = 1750 (a), (b), (e), (f) and Re = 2000 (c), (d), (g), (h) at time $t = 5$. Shown are axial (top) and azimuthal (bottom) projections of the particle configuration for different values of Δ. Lines, symbols, and colors as in Fig. 16.

7. Sensitivity with respect to particle size

For the high-Prandtl-number hydrothermal waves considered, the KAM template is intricate and thus PAS also depends sensitively on the particles size, reflected by the value of Δ. Figure 21 shows side-by-side comparisons of PAS at $t = 5$ for constant Reynolds number and pairwise different interaction parameters. For Re = 1750 and $\Delta = 0.027$ [Figs. 21(a) and 21(e)] about 50% of all particles accumulate near L_1^B [cf. Figs. 16(b) and 16(d) for Re = 1500 and $\Delta = 0.028$]. For the same Reynolds number and the larger interaction parameter $\Delta = 0.04$ [Figs. 21(b) and 21(f)] almost all particles accumulate on the surface of T_8^A [cf. Fig. 12(c)]. For Re = 2000, partial accumulation near L_4^B is found for $\Delta = 0.0195$ [Figs. 21(c) and 21(g)], while almost all particles accumulate around L_1^A for $\Delta = 0.04$ [Figs. 21(d) and 21(h)].

The partial accumulation on the periodic attractors is observed for intermediate values of the interaction parameter $\Delta (\approx 0.01–0.03)$ that are greater than the distance between the free surface and the KAM tori of group B, but less than the distance to the KAM tori of group A, which lie further away from the free surface. For such Δ [see, e.g., Figs. 21(a) and 21(e), and 21(c) and 21(g)] the cylindrical surface at which the PSI takes place intersects with the KAM tori of group B creating the periodic attractor. The KAM tori of group A, on the other hand, do not intersect with the prohibited layer, and the particles moving inside the KAM tori of group A remain confined to these tori [blue dots in Figs. 21(a) and 21(e) and 21(c) and 21(g)]. There are, however, other particles colored in red seemingly randomly distributed within the liquid bridge. These particles stay for a long time (making a large number of revolutions about the axis) on some of the chaotic streamlines between the two groups of KAM tori for Re = 1750 and 2000, especially on those in the vicinity of the regular streamlines, before they experience a PSI. Moreover, after a collision, these particles are
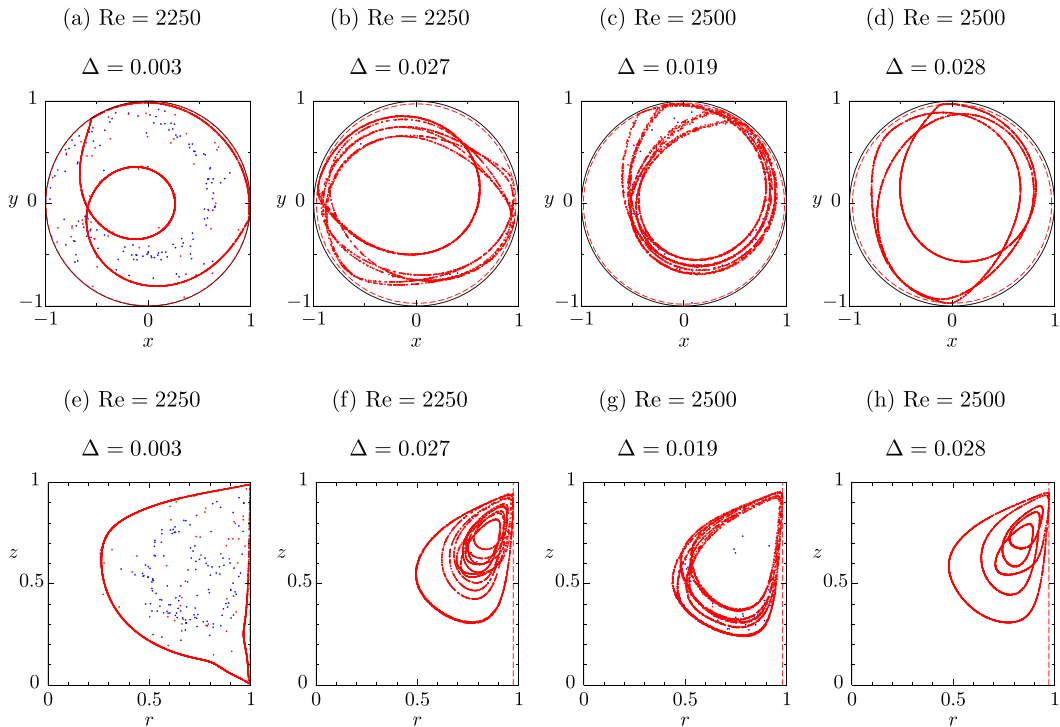
FIG. 22. Examples of PAS in a thermocapillary liquid bridge for $\Gamma = 1$ and Re = 2250 (a), (b), (e), (f) and 2500 (c), (d), (g), (h) at time $t = 5$. Shown are axial (top) and azimuthal (bottom) projections of the particle configuration for different values of Δ. Lines, symbols, and colors as in Fig. 16.

released back to the same chaotic region of the flow. This can lead to confinement of the particles to a chaotic layer near group A even for $t \gg 5$. This is the case for Re = 1750 and $\Delta = 0.027$ [red dots in the diffuse toroidal structure in Figs. 21(a) and 21(e)], and the PAS is classified as strange PAS, similar to that discussed above in the context of Fig. 17 (red dots).

Another scenario is a slow transfer (after many collisions) to the regular streamlines of group B, resulting in a complete accumulation for $t \gg 5$ as happens at $t \approx 15$ for the case of Re = 2000 and $\Delta = 0.0195$ [Figs. 21(c) and 21(g)]. The confinement and persistence of the particles in the chaotic cloud are not yet fully understood, but crucially depend on the mapping among chaotic streamlines upon PSI on which particles move [15,16].

Further examples for periodic and quasiperiodic attractors are provided in Fig. 22 for Re = 2250 and Re = 2500. For Re = 2250 and small particles corresponding to $\Delta = 0.003$, PAS forms in the chaotic region [Figs. 22(a) and 22(e)] with the particle trajectory closed by two PSIs. For larger particles with $\Delta = 0.027$, two periodic attractors can be distinguished: one arises near L_5^A [cf. Fig. 12(b)], while the other one is a trajectory on the KAM torus T_1^B closed by one PSI after one revolution about the axis. For Re = 2500 and $\Delta = 0.019$, Figs. 22(c) and 22(g) show a periodic PAS organized near L_7^B [cf. Fig. 12(h)], while for $\Delta = 0.028$ Figs. 22(d) and 22(h) show a periodic attractor near L_2^A (cf. Fig. 12(g)] with the other line-like attractor being a trajectory on T_1^B closed by one PSI after one revolution about the axis.

V. CONCLUSIONS

The flow structures of traveling hydrothermal waves with a fundamental wave number $m = 1$ and the motion of small spherical particles nearly density matched to the fluid have been numerically

investigated in a cylindrical liquid bridge with Prandtl number $Pr = 68$ and aspect ratio $\Gamma = 1$ under zero gravity conditions. The highly resolved periodic flows have been analyzed in the rotating frame of reference in which the hydrothermal wave is stationary. The flow topology has been characterized in terms of closed streamlines and KAM tori. Some of them approach the free surface sufficiently close to act as organizing centers for the attraction of nearly density-matched particles of particular sizes. Based on the one-way coupling approach, accurate simulations of the motion of a single particle initiated at random positions reveal a rapid accumulation of noninteracting particles.

The KAM structures for $Pr = 68$ and $\Gamma = 1$ are found to be much more intricate than those for $Pr = 4$ [15] and $Pr = 28$ [18]. This allows for nearly density-matched particles of many different sizes to cluster in a rich variety of linelike and tubular PASs of different shapes, which can be well understood based on the underlying KAM template. Among the flow parameters considered, the most intricate KAM structure is found for the lowest thermocapillary Reynolds number considered, $Re = 1500$. The larger the Reynolds number the more the KAM tori become stretched near the free surface due to the high strain rate of the flow. Even for the largest Reynolds number considered, $Re = 2500$, some slender KAM tori have been detected which allow for various PAS to form.

Comparing the two bulk transport models given by pure advection (6) and by the simplified Maxey-Riley equation (7), inertia effects were found to have little impact on PAS formed by small nearly density-matched particles and the parameters considered. Like for $Pr = 28$ [18], the particle-surface interaction proposed by Hofmann and Kuhlmann [14] in their PSI model provides the dissipative mechanism in the dynamical system governing the particle motion which is necessary for the existence of attractors. In this model, kinetic energy of the motion normal to the flow boundary (i.e., the solid walls or free surface) is completely dissipated by a fully inelastic collision when the centroid of the particle has approached the boundary up to the distance Δ. The value of Δ is a model parameter which must be derived from the steric effect the particle experiences when its motion near the free surface is hindered by its own size. In this sense PAS is a dissipative structure which can be classified as a *finite-size coherent structure* (FSCS) [34,47].

Owing to the abundance of closed streamlines and KAM tori in the traveling hydrothermal waves considered, a multitude of finite-size coherent structures of different shapes have been found for density-matched particles and interaction parameters in the range $\Delta \in [0.001, 0.05]$. These values correspond to particle sizes which can be estimated as $a \in [\Delta/2, \Delta]$ [32]. Since we find PASs predominantly near $\Delta \approx 0.037$ and $\Delta \approx 0.007$ (Fig. 15), the most promising particle sizes for PAS can be estimated as $a \in [0.0185, 0.037]$ and $a \in [0.0035, 0.007]$. For a liquid bridge of radius $R = 0.005$ m (planned in the JEREMI space experiment) and $\Gamma = 1$ the corresponding dimensional particle-size ranges are $a_p \in [92.5, 185]$ μm and $a_p \in [17.5, 35]$ μm, respectively. Due to the existence of different attractors even within a small range of Δ (a_p) it seems advisable to use particles in experiments which are highly mono-disperse with respect to their size.

Although the PSI model has been proven successful in capturing the key effect of the finite particle size near the flow boundaries and in predicting PAS, the global parameter Δ remains undetermined in this approach. It would be desirable to determine Δ by additional fully resolving numerical simulation depending on the particle size as was done for a two-dimensional model flow by Romanò and Kuhlmann [32]. Another possibility is softening of the inelastic collision, on which the PSI model is based, by, e.g., incorporating known asymptotic solutions such as the ones of Brenner [33] for a particle in Stokes flow moving near a boundary. A similar approach has recently been used by Romanò *et al.* [34] and Romanò *et al.* [70], who modeled the particle-boundary interaction by the leading-order lubrication approximation for a particle in Stokes flow. Yet another interesting problem relates to the particle dynamics once many particles have accumulated on the same periodic orbit during the final stage of PAS. In this late state of evolution the local particle volume fraction becomes large and particle-particle interaction cannot be disregarded. To date, the effect of the number of particles collected on a periodic single-particle attractor has not been investigated numerically.

ACKNOWLEDGMENTS

[1] N.-S. Cheng, Simplified settling velocity formula for sediment particle, J. Hydraul. Eng. **123**, 149 (1997).

[2] M. J. Olascoaga and G. Haller, Forecasting sudden changes in environmental pollution patterns, Proc. Natl. Acad. Sci. USA **109**, 4738 (2012).

[3] C. T. Crowe, J. D. Schwarzkopf, M. Sommerfeld, and Y. Tsuji, *Multiphase Flows with Droplets and Particles* (CRC Press, Boca Raton, FL, 2011).

[4] S. Holmberg and Y. Li, Modelling of the indoor environment—Particle dispersion and deposition, Indoor Air **8**, 113 (1998).

[5] L. Liu, H. Zheng, L. Williams, F. Zhang, R. Wang, J. Hertzberg, and R. Shandas, Development of a custom-designed echo particle image velocimetry system for multi-component hemodynamic measurements: System characterization and initial experimental results, Phys. Med. Biol. **53**, 1397 (2008).

[6] M. C. Roco, *Particulate Two-Phase Flow*, Butterworth-Heinemann Series in Chemical Engineering (Butterworth-Heinemann, Oxford, 1993).

[7] W. Merzkirch, *Flow Visualization* (Academic Press, Orlando, FL, 1987).

[8] D. Schwabe, P. Hintz, and S. Frank, New features of thermocapillary convection in floating zones revealed by tracer particle accumulation structures (PAS), Microgravity Sci. Technol. **9**, 163 (1996).

[9] S. Tanaka, H. Kawamura, I. Ueno, and D. Schwabe, Flow structure and dynamic particle accumulation in thermocapillary convection in a liquid bridge, Phys. Fluids **18**, 067103 (2006).

[10] D. Schwabe, A. I. Mizev, M. Udhayasankar, and S. Tanaka, Formation of dynamic particle accumulation structures in oscillatory thermocapillary flow in liquid bridges, Phys. Fluids **19**, 072102 (2007).

[11] M. Gotoda, D. E. Melnikov, I. Ueno, and V. Shevtsova, Experimental study on dynamics of coherent structures formed by inertial solid particles in three-dimensional periodic flows, Chaos **26**, 073106 (2016).

[12] A. Toyama, M. Gotoda, T. Kaneko, and I. Ueno, Existence conditions and formation process of second type of spiral loop particle accumulation structure (SL-2 PAS) in half-zone liquid bridge, Microgravity Sci. Technol. **29**, 263 (2017).

[13] M. Gotoda, A. Toyama, M. Ishimura, T. Sano, M. Suzuki, T. Kaneko, and I. Ueno, Experimental study of coherent structures of finite-size particles in thermocapillary liquid bridges, Phys. Rev. Fluids **4**, 094301 (2019).

[14] E. Hofmann and H. C. Kuhlmann, Particle accumulation on periodic orbits by repeated free surface collisions, Phys. Fluids **23**, 072106 (2011).

[15] R. V. Mukin and H. C. Kuhlmann, Topology of hydrothermal waves in liquid bridges and dissipative structures of transported particles, Phys. Rev. E **88**, 053016 (2013).

[16] F. H. Muldoon and H. C. Kuhlmann, Coherent particulate structures by boundary interaction of small particles in confined periodic flows, Physica D **253**, 40 (2013).

[17] D. E. Melnikov, D. O. Pushkin, and V. M. Shevtsova, Synchronization of finite-size particles by a traveling wave in a cylindrical flow, Phys. Fluids **25**, 092108 (2013).

[18] F. Romanò and H. C. Kuhlmann, Finite-size Lagrangian coherent structures in thermocapillary liquid bridges, Phys. Rev. Fluids **3**, 094302 (2018).

[19] I. Barmak, F. Romanò, and H. C. Kuhlmann, Particle accumulation in high-Prandtl-number liquid bridges, PAMM **19**, e201900058 (2019).

[20] J. M. Ottino, *The Kinematics of Mixing: Stretching, Chaos, and Transport*, Cambridge Texts in Applied Mathematics (Cambridge University Press, Cambridge, 1989).

[21] K. Bajer, Hamiltonian formulation of the equations of streamlines in three-dimensional steady flows, Chaos Solitons Fractals **4**, 895 (1994).

[22] F. H. Muldoon and H. C. Kuhlmann, Numerical error in modeling of particle-accumulation structures in periodic free-surface flows, Comput. Fluids **88**, 43 (2013).

[23] D. O. Pushkin, D. E. Melnikov, and V. M. Shevtsova, Ordering of Small Particles in One-Dimensional Coherent Structures by Time-Periodic Flows, Phys. Rev. Lett. **106**, 234501 (2011).

[24] H. C. Kuhlmann and F. H. Muldoon, Particle-accumulation structures in periodic free-surface flows: Inertia versus surface collisions, Phys. Rev. E **85**, 046310 (2012).

[25] D. E. Melnikov and V. Shevtsova, Different types of Lagrangian coherent structures formed by solid particles in three-dimensional time-periodic flows, Eur. Phys. J.: Spec. Top. **226**, 1239 (2017).

[26] P. Capobianchi and M. Lappa, Particle accumulation structures in noncylindrical liquid bridges under microgravity conditions, Phys. Rev. Fluids **5**, 084304 (2020).

[27] M. R. Maxey and J. J. Riley, Equation of motion for a small rigid sphere in a nonuniform flow, Phys. Fluids **26**, 883 (1983).

[28] F. H. Muldoon and H. C. Kuhlmann, Origin of particle accumulation structures in liquid bridges: Particle-boundary-interactions versus inertia, Phys. Fluids **28**, 073305 (2016).

[29] N. Lecoq, R. Anthore, B. Cichocki, P. Szymczak, and F. Feuillebois, Drag force on a sphere moving towards a corrugated wall, J. Fluid Mech. **513**, 247 (2004).

[30] J. C. Brändle de Motta, W.-P. Breugem, B. Gazanion, J.-L. Estivalezes, S. Vincent, and E. Climent, Numerical modelling of finite-size particle collisions in a viscous fluid, Phys. Fluids **25**, 083302 (2013).

[31] C. Pozrikidis, Particle motion near and inside an interface, J. Fluid Mech. **575**, 333 (2007).

[32] F. Romanò and H. C. Kuhlmann, Particle–boundary interaction in a shear-driven cavity flow, Theor. Comput. Fluid Dyn. **31**, 427 (2017).

[33] H. Brenner, The slow motion of a sphere through a viscous fluid towards a plane surface, Chem. Eng. Sci. **16**, 242 (1961).

[34] F. Romanò, P. Kunchi Kannan, and H. C. Kuhlmann, Finite-size Lagrangian coherent structures in a two-sided lid-driven cavity, Phys. Rev. Fluids **4**, 024302 (2019).

[35] S. H. Strogatz, *Nonlinear Dynamics and Chaos* (Perseus Books Group, Cambridge, MA, 1994).

[36] F. Romanò, H. C. Kuhlmann, M. Ishimura, and I. Ueno, Limit cycles for the motion of finite-size particles in axisymmetric thermocapillary flows in liquid bridges, Phys. Fluids **29**, 093303 (2017).

[37] K. Yamaguchi, T. Hori, and I. Ueno, Long-term behaviors of a single particle forming a coherent structure in thermocapillary-driven convection in half-zone liquid bridge of high Prandtl-number fluid, Int. J. Microgravity Sci. Appl. **36**, 360203 (2019).

[38] F. Romanò, H. Wu, and H. C. Kuhlmann, A generic mechanism for finite-size coherent particle structures, Int. J. Multiphase Flow **111**, 42 (2019).

[39] T. Peacock and J. Dabiri, Introduction to focus issue: Lagrangian coherent structures, Chaos **20**, 017501 (2010).

[40] H. Aref, J. R. Blake, M. Budišić, S. S. S. Cardoso, J. H. E. Cartwright, H. J. H. Clercx, K. El Omari, U. Feudel, R. Golestanian, E. Gouillart, G. F. van Heijst, T. S. Krasnopolskaya, Y. Le Guer, R. S. MacKay, V. V. Meleshko, G. Metcalfe, I. Mezić, A. P. S. de Moura, O. Piro, M. F. M. Speetjens *et al.*, Frontiers of chaotic advection, Rev. Mod. Phys. **89**, 025007 (2017).

[41] H. Wu, F. Romanò, and H. C. Kuhlmann, Attractors for the motion of a finite-size particle in a two-sided lid-driven cavity, J. Fluid Mech. **906**, A4 (2021).

[42] H. C. Kuhlmann, F. Romanò, H. Wu, and S. Albensoeder, Particle-motion attractors due to particle-boundary interaction in incompressible steady three-dimensional flows, in *The 20th Australasian Fluid Mechanics Conference*, edited by G. Ivey, T. Zhou, N. Jones, and S. Draper (Australasian Fluid Mechanics Society, Perth, Australia, 2016), p. 102, Paper no. 449.

[43] F. Romanò, S. Albensoeder, and H. C. Kuhlmann, Topology of three-dimensional steady cellular flow in a two-sided anti-parallel lid-driven cavity, J. Fluid Mech. **826**, 302 (2017).

[44] F. Romanò, A. Hajisharifi, and H. C. Kuhlmann, Cellular flow in a partially filled rotating drum: Regular and chaotic advection, J. Fluid Mech. **825**, 631 (2017).

[45] M. Speetjens, G. Metcalfe, and M. Rudman, Lagrangian transport and chaotic advection in three-dimensional laminar flows, Appl. Mech. Rev. **73**, 030801 (2021).

[46] F. Romanò, T. Türkbay, and H. C. Kuhlmann, Lagrangian chaos in steady three-dimensional lid-driven cavity flow, Chaos **30**, 073121 (2020).

[47] F. Romanò and H. C. Kuhlmann, Finite-size coherent structures in thermocapillary liquid bridges, Int. J. Microgravity Sci. Appl. **36**, 360201 (2019).

[48] H. C. Kuhlmann, M. Lappa, D. Melnikov, R. Mukin, F. H. Muldoon, D. Pushkin, V. Shevtsova, and I. Ueno, The JEREMI-project on thermocapillary convection in liquid bridges. Part A: Overview of particle accumulation structures, Fluid Dyn. Mater. Process. **10**, 1 (2014).

[49] S. Matsumoto, K. Nishino, I. Ueno, T. Yano, and H. Kawamura, Marangoni experiment in space, Int. J. Microgravity Sci. **31**, S51 (2014) (in Japanese).

[50] I. Barmak, F. Romanò, P. K. Kannan, and H. C. Kuhlmann, Coherent particle structures in high-Prandtl-number liquid bridges, Microgravity Sci. Technol. **33**, 19 (2021).

[51] P. Capobianchi and M. Lappa, Particle accumulation structures in a 5 cst silicone oil liquid bridge: New data for the preparation of the JEREMI experiment, Microgravity Sci. Technol. **33**, 31 (2021).

[52] A. Babiano, J. H. E. Cartwright, O. Piro, and A. Provenzale, Dynamics of a Small Neutrally Buoyant Sphere in a Fluid and Targeting in Hamiltonian Systems, Phys. Rev. Lett. **84**, 5764 (2000).

[53] Shin-Etsu, *Silicone Fluid KF-96—Performance Test Results*, Tokyo, Japan (2004).

[54] M. Wanschura, V. M. Shevtsova, H. C. Kuhlmann, and H. J. Rath, Convective instability mechanisms in thermocapillary liquid bridges, Phys. Fluids **7**, 912 (1995).

[55] M. Levenstam, G. Amberg, and C. Winkler, Instabilities of thermocapillary convection in a half-zone at intermediate Prandtl numbers, Phys. Fluids **13**, 807 (2001).

[56] J. Leypoldt, H. C. Kuhlmann, and H. J. Rath, Three-dimensional numerical simulation of thermocapillary flows in cylindrical liquid bridges, J. Fluid Mech. **414**, 285 (2000).

[57] J. Leypoldt, H. C. Kuhlmann, and H. J. Rath, Stability of hydrothermal-wave states, Adv. Space Res. **29**, 645 (2002).

[58] M. Orlishausen, L. Butzhammer, D. Schlotbohm, D. Zapf, and W. Köhler, Particle accumulation and depletion in a microfluidic Marangoni flow, Soft Matter **13**, 7053 (2017).

[59] C. F. M. Coimbra and R. H. Rangel, Spherical particle motion in harmonic Stokes flows, AIAA J. **39**, 1673 (2001).

[60] W.-P. Breugem, A combined soft-sphere collision/immersed boundary method for resolved simulations of particulate flows, in *Proceedings of the ASME 2010 3rd Joint US-European Fluids Engineering Summer Meeting and 8th International Conference on Nanochannels, Microchannels, and Minichannels* (ASME, Montreal, Canada, 2010), p. FEDSM-ICNMM2010-30634.

[61] H. C. Kuhlmann and T. Lemée, *Particle Accumulation in the JEREMI Experiment: Definition of Necessary Flow and Particle Parameters (PARTAC)—Final Report*, FFG Report (ASAP) Project no. 840119 (TU Wien, Vienna, 2016).

[62] J. Dormand and P. Prince, A family of embedded Runge–Kutta formulae, J. Comput. Appl. Math. **6**, 19 (1980).

[63] M. Stojanovic and H. C. Kuhlmann, Stability of thermocapillary flow in high-Prandtl-number liquid bridges exposed to a coaxial gas stream, Microgravity Sci. Technol. **32**, 953 (2020).

[64] M. K. Smith, Instability mechanisms in dynamic thermocapillary liquid layers, Phys. Fluids **29**, 3182 (1986).

[65] H. G. Schuster, *Deterministic Chaos: An Introduction* (Wiley-VCH, Weinheim, 2005).

[66] M. Gotoda, T. Sano, T. Kaneko, and I. Ueno, Evaluation of existence region and formation time of particle accumulation structure (PAS) in half-zone liquid bridge, Eur. Phys. J.: Spec. Top. **224**, 299 (2015).

[67] H. C. Kuhlmann and T. Lemée, Particle-depletion dynamics in axisymmetric thermocapillary flows, Eur. Phys. J.: Spec. Top. **224**, 309 (2015).

[68] H. C. Kuhlmann and F. H. Muldoon, On the different manifestations of particle accumulation structures (PAS) in thermocapillary flows, Eur. Phys. J.: Spec. Top. **219**, 59 (2013).

[69] F. Romanò and H. C. Kuhlmann, Numerical investigation of the interaction of a finite-size particle with a tangentially moving boundary, Int. J. Heat Fluid Flow **62**, 75 (2016).

[70] F. Romanò, P.-E. des Boscs, and H. Kuhlmann, Forces and torques on a sphere moving near a dihedral corner in creeping flow, Eur. J. Mech. B **84**, 110 (2020).